Theoretical investigations of bulk and surface properties of group II and group XII metal fluorides

Inaugural-Dissertation
to obtain the academic degree
Doctor Rerum Naturalium (Dr. rer. nat.)

submitted to
the Department of Biology, Chemistry and Pharmacy
of Freie Universität Berlin

by

Zeinab Kaawar

from Beirut

2018

This work was prepared under supervision of
Prof. Dr. Beate Paulus (Freie Universität Berlin)
from March 2013 until March 2018

1. Reviewer: Prof. Dr. Beate Paulus

2. Reviewer: Prof. Dr. Erhard Kemnitz

Date of the Defense: 02.05.2018

Acknowledgments

This thesis would not have been possible without the contributions of many people I encountered during my doctoral studies, and who have made this time an unforgettable experience for me. It is my pleasure to thank all of them.
First and foremost, I would like to express my special appreciation and gratitude to my supervisor, Prof. Dr. Beate Paulus for her support and guidance during my entire doctoral thesis. She offered me the opportunity to do a research internship in her group, where I learned a lot in theoretical chemistry, and allowed me to pursue my PhD and work on this exciting research topic. I am grateful for the chances given by her to attend conferences and workshops, which broadened my scientific expertise. I enjoyed working with her, and discussing together many topics - not only about science.
I would like to thank Prof. Dr. Erhard Kemnitz for his vivid interest in my research, the fruitful discussions I had with him and for willingly accepting the task of being the second referee of my thesis.
I am grateful to Dr. Lukas Hammerschmidt who helped me since the beginning of my research internship in the Paulus group. He has kindly listened to my problems and was always opened for questions. Dr. Carsten Müller, who provided me with a broad range of informations, I would like to thank for his help in many practical problems and the productive discussions throughout my thesis. Dr. Elisaveth Kanaki, with whom I shared the office for about two years, has been very supportive and inspiring for my work, has gladly helped me and has brightened me up in difficult moments. Dr. Matthias Berg has offered me valuable support and was always there for any help.
Among the people who contribute to ensure the smooth working of a university, I am grateful to Julija Djordjevic for her help with administrative issues, and to the ZEDAT-team for technical support. I gratefully acknowledge financial support from Erasmus-Mundus and from the Deutsche Forschungsgemeinschaft (DFG) through the graduate school "Fluorine as a key element" and thank HLRN (North-German Super-computing Alliance) for computational time.
For the enjoyable and productive working environment, I would like to thank all my colleagues in the theoretical chemistry groups (AG Paulus, AG Tremblay and AG Keller), especially Dr. Andreas Achazi and Stefan Mattson.
I would like to thank Dr. Susan Torabi and Dr. Krista Steenbergen for the discussions and their help. Also, I enjoyed the exchange with Dr. Larissa Schmidt, Dr. Alexander Rehmer and Stefan Mahn from the Humboldt University.
For making my time in Berlin memorable and being always available whenever I needed support, I would like to thank my dearest friends Yasmeen Qawasmeh and Maysoon Saleh. They

offered me valuable advices, patiently listened to my problems and encouraged me when I was depressed. Together, we have shared many unforgettable moments, in and outside the university.
Most of all, I am very grateful to my small family: to my husband Ali who has always been and will always be an important part of my life. My thesis could not have been successful without his support and understanding during my whole doctoral trip. To my little children Fatima and Hussein, who beared long days stays away from their Mom, I say: “You are the most precious gift God gave me.”
Last but not the least, it is hard to express in words my gratitude towards my parents. They were and still are the source of my success in life. The best way to thank them and repay their unconditional love and trust is to keep doing my best in all I do.

Abstract

Nanoscopic metal fluorides are of current interest in surface chemistry, as well as in optics and dentistry. Synthesized via the fluorolytic sol-gel procedure, they have shown to exhibit high surface area and to act as Lewis acids, due to the presence of coordinatively unsaturated cations on the surface. In this thesis, a variety of divalent metal fluorides, including zinc, calcium, strontium and barium fluorides, are investigated in different directions. Starting with zinc fluoride crystal, the bulk and surface structure of the rutile and $CaCl_2$ modifications are examined by means of first principle calculations. The shape of the crystal in vacuum is predicted using the Wulff construction. In a way towards the understanding of the missing catalytic activity of sol-gel synthesized zinc fluoride nanomaterials compared to magnesium fluoride, as it has been shown by our experimental partners, the Lewis acidity of coordinatively unsaturated surface cations of rutile ZnF_2 is investigated by modeling the adsorption of carbon monoxide on the low-index surfaces. Adsorption energies are calculated using density functional, Hartree-Fock and local Møller-Plesset perturbation theory (LMP2) for the periodic systems. The results show that the strength of the adsorption, which is a measure of the Lewis acidity, does not only depend on the number of missing coordination partners of the surface cations. Moreover, the reactivity of the surfaces is not uniquely determined by the Lewis acidity of the cationic sites, but the surface composition and the anions on the surface are of importance too. From a methodological perspective, DFT was shown to be adequate for a good description of CO adsorption, performing well compared to LMP2, while dispersion corrections on DFT strongly overestimate the adsorption energies.
The bulk and surface properties of group II metal fluorides CaF_2, SrF_2 and BaF_2, in fluorite crystal structure, are also studied in this work using periodic DFT calculations. Adsorption of hydrogen fluoride on low-index MF_2 (M = Ca, Sr, Ba) surfaces is modeled at different coverages, using different computational methods. PBE and PBE0 are found to perform similarly for the adsorption structures and energies, both predicting a chemisorption in most cases with the adsorption strength increasing upon lowering coverage. Combining the quantum chemical results with surface thermodynamics, the stability of different terminations under temperature and pressure of hydrogen fluoride is analyzed. Using the Wulff construction, the shape of the crystals at finite conditions of temperature and hydrogen fluoride pressure is derived. The outcomes of these investigations suggest that all three materials expose clean surfaces at high temperature and surfaces covered with HF at low temperature. The predicted shapes of CaF_2 and SrF_2 nanocrystals are in good agreement with TEM images of sol-gel synthesized nanocrystals at room temperature and high excess of hydrogen fluoride.

Zusammenfassung

Nanoskopischen Metallfluoriden gilt aktuelles Interesse in der Oberflächenchemie, der Optik und der Zahnmedizin. Dargestellt über die fluorolytische Sol-Gel-Synthese, weisen diese große Oberflächen auf und agieren, auf Grund von koordinativ ungesättigten Oberflächenkationen, als Lewis-Säuren. In dieser Arbeit werden eine Vielzahl divalenter Metallfluorid, namentlich Zink-, Calcium-, Strontium- und Bariumfluorid, unter verschiedenen Gesichtspunkten untersucht. Zuerst werden die Kristall- und Oberflächenstrukturen der Rutil- und $CaCl_2$- Modifikationen des Zinkfluorids mittels *first principle* Berechnungen untersucht. Die Vorhersage der Form des Kristalls im Vakuum erfolgt über die Methode der Wulff-Konstruktion. Um die, im Vergleich zu Magnesiumfluorid, fehlende katalytische Aktivität Sol-Gel synthetisierter Zinkfluorid-Nanomaterialien, wie von unseren experimentellen Partnern demonstriert, zu verstehen, wird die Lewis-Azidität von koordinativ ungesättigten Oberflächenkationen der Rutilstruktur des ZnF_2 untersucht. Dafür wird die Adsorption von Kohlenstoffmonoxid auf niedrig indizierten Oberflächen modelliert. Die Berechnung der Adsorptionsenergien der periodischen Systeme erfolgt mittels der Dichtefunktionaltheorie, des Hartree-Fock-Verfahrens, sowie der lokalen Møller-Plesset Störungstheorie (LMP2). Die Ergebnisse zeigen, dass die Stärke der Adsorption, ein Maß für die Lewis-Azidität, nicht ausschließlich von der Anzahl an fehlenden Koordinationspartnern der Oberflächenkationen abhängt. Überdies ist die Reaktivität der Oberflächen nicht eindeutig über die Lewis-Azidität der kationischen Gitterplätze bestimmt, da auch die Zusammensetzung der Oberfläche und die Oberflächenanionen von Bedeutung sind. Im Hinblick auf die verwendeten Methoden, kann durch den Vergleich mit LMP2 gezeigt werden, dass die Adsorption von CO gut mit DFT beschrieben wird, während die Verwendung von DFT mit Dispersionskorrekturen zu einer Überschätzung der Absorptionsenergien führt. Des Weiteren werden in dieser Arbeit die Kristall- und Oberflächeneigenschaften der Gruppe II Metallfluoride CaF_2, SrF_2 und BaF_2, in der Fluorit-Kristallstruktur, mittels periodischer DFT-Rechnungen untersucht. Die Adsorption von Fluorwasserstoff auf niedrig indizierten MF_2 (M = Ca, Sr, Ba) Oberflächen wird für verschiedene Bedeckungsgrade und mit unterschiedlichen DFT-Methoden modelliert. PBE und PBE0 liefern ähnliche Ergebnisse bezüglich der Adsorptionsstrukturen und -energien. Beide Methoden sagen für die meisten Fälle Chemisorption vorher, wobei die Adsorptionsstärke bei abnehmenden Bedeckungsgraden zunimmt. Die Kombination der quantenchemischen Resultate mit den Methoden der Oberflächenthermodynamik erlaubt die Bestimmung der Stabilität verschieden terminierter Oberflächen in Abhängigkeit der Temperatur und des Fluorwasserstoffdrucks. Mittels Wulff-Konstruktion wird die Form der Kristalle bei endlicher Temperatur und endlichem Fluorwasserstoffdruck ermittelt. Die Ergebnisse dieser Untersuchungen legen nahe, dass alle drei Materialien bei

hohen Temperaturen freie Oberflächen und bei niedrigen Temperaturen mit HF bedeckte Oberflächen aufweisen. Die vorhergesagten Formen der CaF_2 und SrF_2 Nanokristalle stimmen gut mit den TEM Aufnahmen von Sol-Gel synthetisierten Nanokristallen bei Raumtemperatur und großem Fluorwasserstoff-Überschuss überein.

List of Publications

P1 Z. Kaawar and B. Paulus
A computational Study of the Structure of Zinc Fluoride Surfaces
AIP Conf. Proc., **1653**, 020051 (2015)
DOI: 10.1063/1.4914242

P2 Z. Kaawar, C. Müller and B. Paulus
Theoretical investigations of the CO adsorption on ZnF_2 surfaces
Surface Science, **656**, 48-53 (2017)
DOI: 10.1016/j.susc.2016.06.021

P3 Z. Kaawar, S. Mahn, E. Kemnitz and B. Paulus
On the morphology of Group II Metal Fluoride Nanocrystals at Finite Temperature and Partial Pressure of HF
Molecules, **22**, 663 (2017)
DOI: 10.3390/molecules22040663

P4 Z. Kaawar and B. Paulus
Adsorption of hydrogen fluoride on alkaline earth fluoride surfaces: a first-principles study
Will be submitted soon to "Journal of Fluorine Chemistry"

Contents

List of Figures

List of Tables

1 Introduction

A highly investigated, fast developing and vastly advertised topic nowadays is "Nanomaterials". This term is devoted to materials having a size range of 1 to 100 nm, at least in one spatial dimension. The study of nanomaterials requires a basic understanding of chemistry and physics, some knowledge of materials science and - because of many interesting applications - also of biology and medicine. The concept of nanotechnology was first introduced by P. Feynman in 1959, in his famous speech "There's plenty of room at the bottom" [1], meaning that "the control of materials and their properties in the atomic scale comprised a new frontier of opportunity in science and technology". About 30 years later, Gleiter et al. launched the systematic study of nanoscopic materials, introducing the terms "nanocrystalline" and "nanocrystal" [2]. Due to their size-dependent physical and chemical properties [3], nanomaterials are spread over a wide range of applications in many areas of human activity, particularly in electronics [4–7], optics [8, 9] and medicine [10–12]. An attractive example of such materials are metal fluorides [13–15]. For a long period of time, the interest in metal-based compounds was confined to oxides [16–18]. Only recently, a considerable attention has been devoted to metal fluorides, especially after the development of the sol-gel route to their synthesis [19]. Originally used for the synthesis of nanoscopic AlF_3 [20–22] and successfully applied to MgF_2-based materials [23], the fluorolytic sol-gel synthesis has been operated on many other fluorides [24], including ZnF_2 [25] and the alkaline-earth fluorides CaF_2, SrF_2 and BaF_2 [26, 27]. In a sol-gel procedure (see Fig. 1.1), a metal precursor reacts with hydrogen fluoride in a suitable organic solvent to form a transparent sol. After a post-treatment the desired nanomaterial is obtained.

1.1 Synthesis and applications of metal fluoride nanocrystals

Due to their high surface area and moderate to high Lewis acidity, the sol-gel synthesized aluminium fluoride and magnesium fluoride have revealed outstanding catalytic performance with high activity as well as high selectivity for a broad range of chemical reactions [19, 29–37], like for example the fluorination of 2-chloropyridine to 2-fluoropyridine [38]. They have also shown excellent applicability in antireflective optical coatings [39], where metal fluorides

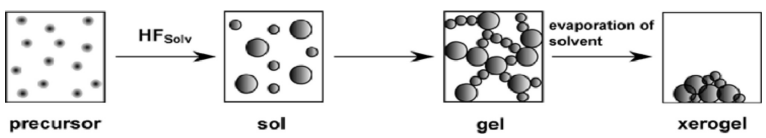

Figure 1.1: Pictorial representation of a sol-gel procedure [28].

based thin films of high mechanical resistance were obtained. Moreover, they are used as inorganic components embedded in an organic polymer matrix to form composite materials with new functionalities [40]. These advantageous properties offered a motivation and paved the way towards the synthesis of further nanoscopic metal fluorides. Due to the similarity between Zn and Mg in terms of electron configuration, coordination number and ionic radius [41], ZnF_2 was chosen as a primary research target and was prepared via the sol-gel synthesis route [25]. This proceeds by the reaction of zinc acetate with hydrogen fluoride to form a colloidal suspension of solid nanoparticles. Upon aging and drying, the final product is formed. The synthesis of ZnF_2 is performed under both non-aqueous and aqueous conditions to test the effect of water in the synthesis process. It was found out that the presence of water leads to a higher fluorination degree in the prepared compounds, and therefore crystallization is favoured. Partial hydroxylation of the surface, which occured in the synthesis of MgF_2, was not observed on ZnF_2. The sol-gel prepared ZnF_2 has a significantly high surface area and the estimated average diameter of the sol particle is about 16 nm, which indicates its nanoscopic nature. ZnF_2 is predominantly a Lewis acidic solid with some weak Lewis basic sites [25].

Several synthetic routes to nanoscopic alkaline earth metal fluorides were employed, namely the reverse micelle method, solvothermal process, different precipitation methods, the mechanochemical route and the sol-gel fluorination [42–55]. A mechanochemical synthesis of nanocrystalline CaF_2, SrF_2 and BaF_2 has been described recently [54]. Using metal carbonates, acetates or hydroxides as educts and ammonium fluoride as fluorinating agent, phase pure nanocrystalline metal fluorides are formed by milling in a planetary mill. Moreover, simple manual shaking reactions of ammonium fluoride with the metal hydroxides result in exclusively crystalline metal fluorides. The nanocrystalline samples prepared via this method have a size of about 10 nm and exhibit high fluorine ion conductivity. Alkaline earth fluorides with high surface area and tunable surface properties are obtained in a fluorolytic sol-gel synthesis. Rehmer et al. [26] reported the synthesis of nanoscopic CaF_2 via the sol-gel process to prepare antireflective CaF_2-films by dip-coating. For this purpose, they used calcium chloride as a precursor and reacted it with anhydrous hydrogen fluoride in ethanol. The prepared CaF_2-films exhibit an excellent optical performance as well as a good mechanical stability, and show a small particle diameter in the range of 10 to 20 nm. An alternative synthetic route starting with calcium lactate dissolved in a mixture of lactic acid and formic acid and adding an aqueous solution of hydrogen fluoride, has been described also [56]. Similar to CaF_2, the reaction of strontium lactate with aqueous hydrogen fluoride results in SrF_2 nanocrystals. In both cases, the solid obtained possesses a high surface area and a nanoscopic nature, with the size of the nanocrystals ranging between 5 and 20 nm. However, in the case of CaF_2 clearly a cubic shape of all nanocrystals is observed, whereas for SrF_2 mostly spherical looking nanocrystals are obtained. Additionally, SrF_2 nanoparticles were synthesized also via the sol-gel route, using strontium acetate hemihydrate as precursor and non-aqueous HF solution as fluorinating agent [27]. The resulting nanocrystals were found to have a crystallite size below 10 nm, and crystal lattice planes of nano-SrF_2 were observed in a high-resolution transmission electron microscopic image, proving the crystallinity of the

particles. For the synthesis of BaF_2, barium methoxide is reacted with hydrogen fluoride in methanol yielding a high surface area BaF_2 nanocrystal [55]. Experiments on the characterization of the acidity and the basicity of the prepared materials show the presence of medium Brønsted acidic sites in calcium fluoride and strontium fluoride, whereas barium fluoride possesses weak Lewis acidic sites and strong Lewis basic sites [57].

Sol-gel synthesized nanoscopic metal fluorides are characterized by exceptional properties, like high surface area and high reactivity, which makes them very promising candidates in heterogeneous catalysis. For example, alkaline earth fluorides catalyze the dehydrohalogenation of chlorofluorobutanes, with BaF_2 showing an interesting catalytic activity with high selectivity for the dehydrochlorinationtion of 3-chloro-1,1,1,3-tetrafluorobutane [57]. ZnF_2 combined with chiral diamine ligands has been found to exhibit a high catalytic activity for the asymmetric allylation of acylhydrazono esters [58]. In addition to the catalytic properties, nanoscopic metal fluorides exhibit excellent optical properties which allow wide-ranging applicability in the field of optics, mainly anti-reflective coatings, spectroscopy and laser applications. ZnF_2 is one of the important optical materials which can exhibit different optical properties upon doping. It presents a large anisotropy in its dielectric properties when doped with lithium [59], which makes it a good candidate for optical device manufacturing. Another attractive feature is an effective electroluminescense in rare-earth doped bulk crystals and polycrystalline films of ZnF_2, being therefore a promising compound for electroluminescent device applications [60]. For example, ZnF_2 thin films doped with trivalent rare-earth ions, such as Ce, Nd, Sm, Eu and Er, show an electroluminescent emission from UV to blue regions [61]. ZnF_2 has also driven much interest in vacuum ultraviolet photo-electron spectroscopy due to its wide band gap [62]. BaF_2 is considered as the fastest luminescent material [63] and is widely used for γ-ray and elementary particle detection [64]. By dissolving appropriate impurities into its lattice, BaF_2 exhibits superionic conductivity which makes it a promising material for high-temperature batteries, chemical filters and sensors [65]. CaF_2 and SrF_2 are often used as chemical-resistant, weather-proof coating materials for high quality optical windows [26, 27, 39], due to their low refractive index and their low solubility in water [66]. They are also used as ceramic laser materials because of their excellent mechanical and optical properties [67]. Furthermore, divalent metal fluorides play a crucial role in dental applications [68, 69], by preventing and controlling dental caries. Used as inorganic fillers in dental composites, CaF_2 and SrF_2 improve the mechanical and chemical properties of dental materials since they also act as fluoride-releasing materials, which is of high importance in caries prevention.

Motivated by the outlined diversity in applications of the sol-gel prepared metal fluorides and the versatile path to their synthesis, I aim in this project at developing a predictive model for a group of metal fluorides, through investigating their structure, composition and properties and understanding the relationship between them. The focus is on two different systems: Zinc fluoride (ZnF_2) in rutile structure and group II fluorides including calcium, strontium and barium fluorides (CaF_2, SrF_2 and BaF_2) in fluorite structure.

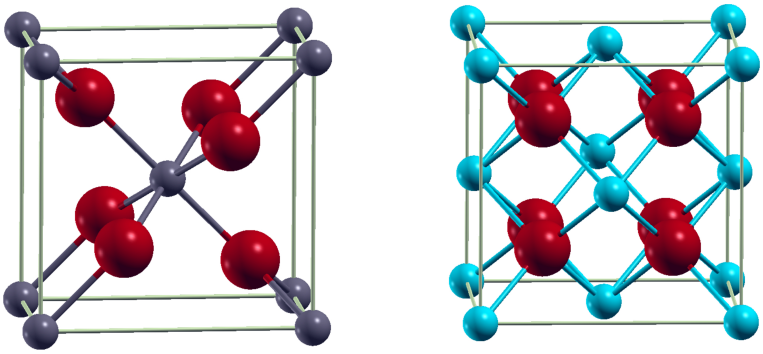

(a) (b)

Figure 1.2: Bulk unit cells of (a) ZnF_2 and (b) CaF_2. Zinc atoms are represented as grey, calcium as blue and fluorine as red spheres.

1.2 Bulk and surface characteristics

1.2.1 Nanostructured zinc fluoride

Zinc fluoride crystallizes in the tetragonal rutile structure with space group 136 ($P4_2/mnm$) and two ZnF_2 formula units in the conventional unit cell (see Fig. 1.2). In the bulk, each zinc cation is surrounded by six fluorine anions in an octahedral arrangement, while each anion is coordinated to three cations. So, an octahedron is formed by one zinc ion in the center and six fluorine ions in the corners. The neighboring octahedra are connected to each other through an edge-shared F anion. The lattice constants of rutile-type ZnF_2 obtained from X-ray powder diffraction are $a = 4.703$Å and $c = 3.133$Å, and the relative coordinate of the fluorine ion is $x(\mathrm{F}) = 0.305$ [70].
Pressure induced phase transitions occuring in solids are of great importance since they affect the structural and electronic properties of the material. A ZnF_2 crystal undergoes a phase transition from the rutile-type to the $CaCl_2$-type structure at a pressure of about 4.5GPa, and to the PdF_2-type for pressures above 6.5GPa [71]. The rutile and the $CaCl_2$ structures are very similar, in terms of bulk properties and surface energies, besides the fact that they belong to different lattice systems, tetragonal and orthorhombic [72].
It is well known that the surface acid-base properties of metal fluorides influence their potential as heterogeneous catalysts. Indeed, acidic fluorides with high surface area are very promising candidates in heterogeneous catalysis, and thus, knowing the Lewis acidity of the surface cations is crucial for understanding the catalytic performance of the material. Compared to the structurally similar MgF_2, ZnF_2 has the same type of unsaturated surface cations, being slightly weaker in both acidity and basicity. However, in contrast to the large catalytic activity of MgF_2 based materials, ZnF_2 did not show any catalytic potential for the dismutation reaction of chlorofluoromethanes. In this context, a question arises: Is this lack of catalytic activity mainly related to a different structure of ZnF_2 crystallites or to a lower activity of surface sites?

1.2.2 Group II metal fluorides

The bulk and surface properties of alkaline earth fluorides CaF_2, SrF_2 and BaF_2 are widely investigated in experimental as well as in theoretical studies [73–77]. These materials are highly ionic insulators which crystallize in the cubic fluorite structure of space group 225 ($Fm\bar{3}m$). The unit cell consists of three ions, one cation chosen as origin, and two anions placed at $\pm(1/4, 1/4, 1/4)$. Each cation is surrounded by 8 equidistant anions situated at the corners of a cube, with the cubes edge-connected in a face centered cubic array, and each anion has 4 neighboring cations arranged in a regular tetrahedron [78] (see Fig. 1.2). Data from X-ray powder diffraction estimates the lattice constant to be 5.46, 5.80 and 6.20Å for CaF_2, SrF_2 and BaF_2, respectively [79–83].

Synchroton-radiation studies of CaF_2 at high pressures show that a phase transition from the fluorite to the orthorhombic $PbCl_2$-type structure occurs at about 9.5GPa [84]. Tight binding linear muffin tin orbital calculations confirm that the group II fluorides CaF_2, SrF_2 and BaF_2 undergo a phase transition to the orthorhombic structure at transition pressures of 9.1, 7.0 and 2.84GPa, respectively [85, 86]. In the case of BaF_2, a second phase transition is induced for a pressure as high as 12.8GPa, where the orthorhombic $PbCl_2$-type structure transforms into a hexagonal Ni_2In-type structure. Upon compression, the three materials are predicted to undergo insulator to metal transition at metallization pressures of nearly 210, 91 and 33GPa for CaF_2, SrF_2 and BaF_2, respectively [85, 86].

The electronic structure of the materials under study has been extensively investigated and reported in a number of publications. Experimental studies based on vacuum-ultraviolet spectroscopy estimate the indirect band gaps of CaF_2, SrF_2 and BaF_2 to be 11.18, 10.60 and 10.00eV, respectively [87]. Kanchana *et al.* [85, 86] have shown, in a DFT study using the LDA functional, that calcium, strontium and barium fluorides are wide band gap insulators with the gap occuring between the "p" like valence band of the fluorine and the "sd" like conduction band of the metal. They reported indirect band gap values of 7.24, 7.5 and 7.033eV for CaF_2, SrF_2 and BaF_2, respectively. In another work based on DFT calculations using the hybrid B3PW functional [88, 89], the calculated band gap was 10.68eV for CaF_2 and 11.30eV for BaF_2, in a very good agreement with the experimental values. It has also been shown that the charge density between atoms in the bulk crystal is very small reflecting the high ionic nature of the metal-fluorine chemical bonding.

The natural cleavage plane of a MF_2 (M = Ca, Sr or Ba) crystal is the (111) surface, which consists of planes of metal ions in a hexagonal array with a layer of fluoride ions both above and below. The (111) surface is thus terminated with fluoride ions and just below the surface are seven-fold coordinated metal ions [90]. The energy required to create this surface is 0.45 J/m^2 for CaF_2 [91]. There exist two other low index surfaces of higher surface energy, the (110) and the (100) surfaces. The three surfaces were investigated in this thesis, with the help of periodic slab calculations. I analyze in detail the surface structure and calculate surface energies which give insights about the stability and allow a prediction of the nanocrystal shape.

The reactivity of calcium fluoride surfaces has been experimentally investigated by several

research groups, mainly through water vapor adsorption experiments. An early study using the infrared technique [92] shows that water is chemisorbed on the CaF_2 surface and the adsorbed water molecules are strongly bound to each other. In the same study, it has been shown that the surface of BaF_2 is not able to bind adsorbed water molecules and adsorption of water vapor on this surface is brought by a physisorption process. De Leeuw et al. [93] published a theoretical study dealing with the adsorption of water and methanoic acid on the (111) surface. Their DFT calculations within the generalized-gradient approximation show that the most stable configuration of water on the (111) surface is an associative adsorption without any dissociation of the water molecules to form a hydroxylated surface. The calculated hydration energies and their decrease with increasing coverage suggest the difficulty of accomodating a full monolayer of water molecules, due to the small lattice spacing of calcium, and indicate the presence of repulsive interactions between the adsorbates. The same trends were observed for the adsorption of methanoic acid which adsorbs by its oxygen to two calcium atoms forming a bridge between them. The adsorption of methanoic acid was found to be energetically more favorable compared to water adsorption. In this work, I study the adsorption of hydrogen fluoride molecules on the low-index surfaces (111), (110) and (100) of MF_2 at different coverages. I evaluate the adsorption structures and energies which give valuable information about the strength of the interaction between the surface and the adsorbate. This is of importance for the formation of the nanomaterial since hydrogen fluoride is a reactant in the synthetic route.

1.3 Quantum chemical modeling of metal fluorides

Solids can be modelled in quantum mechanics using two different approaches: embedded clusters and periodic models. The embedded clusters scheme consists of dividing the bulk system into two parts: a small finite fragment (cluster) which is explicitly treated in quantum chemical calculations, and the surrounding bulk, which is often neglected. This approach is usually used for modeling non periodic solids. The periodic model allows a structural description of the system by a small part of it, the unit cell, which features a translational symmetry. The periodic approach has been employed in modeling the bulk crystals and the surfaces in this thesis and is therefore explained in detail in the next chapter.
The process of adsorbing small molecules on the surfaces of crystalline solids is recognized as a powerful tool for the characterization of surface properties, such as Lewis acidity. This is of great importance in many fields of surface science, mainly in surface catalytic reactions. Depending on the strength of the interaction between the surface and the adsorbate, adsorption is classified into two types: chemisorption in which the molecular electronic structure of the adsorbent is perturbed and chemical bonds are formed with the substrate, and physisorption which retains the electronic structure of the molecule with some small distortion. The latter case is governed by weak dispersion interactions which are caused by interactions in the fluctuating polarizations of surface and adsorbate [94]. To treat these interactions, it is necessary to account for electron correlation. While Hartree-Fock theory lacks electron correlation, modern wave-function based post-HF methods include electron correlation and

are successfully applicable to small sized systems, but are difficult to apply on extended systems.

Density functional theory is widely used for the description of adsorption processes on surfaces [95, 96], due to the compromise between accuracy and computational cost. However, standard density functionals often fail to correctly describe electron correlation and therefore dispersion effects [97–101]. Especially for systems where weak interactions are important, DFT with standard functionals does not yield the desired accuracy. A variety of attempts to account for this inadequacy has been proposed [102–109]. Dispersion correction schemes based on empirical approaches have been introduced by Grimme [108, 109], and successfully applied to adsorption systems [110–113]. Based on sophisticated calculations with the use of approximations, the Grimme corrections improve very efficiently on the accuracy. They are implemented in quantum chemical codes for molecules as well as for solids and are therefore widely used. In this thesis, I apply the Grimme corrections (D2 and D3) to the DFT calculations of adsorption interactions, and thus, I discuss the method in detail in the next chapter.

A number of wave function-based methods has been put forward to accurately determine the correlation contributions. These comprise configuration interaction [114], coupled cluster schemes [115] and Møller-Plesset perturbation theory (MP_n) of order n [116], which are very productive for small systems, but become nearly impractical for extended systems due to their exponential scaling with the system size [117]. To remedy this problem and reduce the computational cost, approaches based on a localized orbital representation are employed. The so-called local ansatz originally introduced by Stollhoff and Fulde relies on excitations out of non-orthogonal localized orbitals [118–120]. Later, Pulay and Saebo [121–123] employed localized orthogonal orbitals to represent the occupied HF manifold and non-orthogonal projected atomic orbitals (PAOs) to describe the virtual space. This scheme was applied by Werner and Schütz to molecular systems and was implemented in the MOLPRO program [124, 125]. Pisani et al. [126, 127] extended the use of the local approach to solids, which was implemented in the CRYSCOR code [127, 128]. A slightly different scheme, called the method of increments (MoI), was proposed by Stoll for extended systems [129–132]. Relying on clusters, the electron correlation energy obtained from the MoI consists of a many-body expansion, in a way that allows the truncation of the virtual space. It has been shown recently that periodic local second-order Møller-Plesset perturbation theory (LMP2) is sufficient for an accurate description of metal fluorides [133], yielding very good results in comparison with the MoI using CCSD(T). Therefore, in this thesis, I employed the periodic LMP2 theory to study adsorption of CO on ZnF_2 surfaces (see Paper P2).

1.3.1 Predictive modelling of the crystal shapes

It is well known that chemical reactions are strongly influenced by temperature and pressure. The later are not included in *ab initio* calculations and therefore all calculated physical properties are only valid at $T = 0$K and $p = 0$atm. However, *ab initio* calculations can be combined with thermodynamics to include the effects of temperature and pressure. This

combination, referred to as *ab initio* surface thermodynamics, is employed to link results from quantum chemical calculations to macroscopic properties and predict the stability of different surfaces under realistic conditions. The method was established and applied to metals and metal oxides in contact with an oxygen gas phase [134–136]. A good agreement with experimental findings was achieved for ruthenium and palladium metals as well as their corresponding oxides [134, 136, 137]. Later, with the development of the fluorolytic sol-gel synthesis, surface thermodynamics were employed to predict the stability of AlF_3 [138] and MgF_2 surfaces in a mixed HF/H_2O environment [139].
Ab intio surface thermodynamics have the advantage of providing an insight in the formation of the surfaces at a relatively low computational cost. The procedure is as follows: given a set of quantum chemically calculated structures, their thermodynamic stability can be evaluated over a broad range of temperature and pressure conditions, through calculating the Gibbs surface energy. Based on that, I employed surface thermodynamics in the present work to model the influence of the temperature and the pressure of HF on the stability of low index MF_2 surfaces and therefore predict the morphology of the nanocrystals under different conditions.

2 Theory and methodology

In 1900, Max Planck developed a theory, the so-called blackbody radiation, to study the light emitted by heated solids. His work was considered to mark the beginning of quantum mechanics [140]. After about 25 years, Heisenberg, Born and Jordan [141] had developed a complete and consistent theory of quantum mechanics, called matrix mechanics. A few months later, Erwin Schrödinger introduced the concept of the wave function and the equation governing its change with time to describe the state of a system in quantum mechanics [142]. The time-dependent Schrödinger equation is written as

$$i\frac{\partial}{\partial t}\,\Psi(x,t) = \hat{H}\Psi(x,t), \tag{2.1}$$

where $\Psi(x,t)$ represents the wave function that contains all possible information about a quantum system. It is a function of time t and of space coordinates x of all quantum mechanically described particles in the system. $\hat{H}$ is the Hamiltonian that corresponds to the total energy of the system, which is conserved.
Because of its complexity, the Schrödinger equation could not be solved, for systems exceeding two particles, unless approximations are introduced. As a first approximation, the time- and the spatial-dependence of the wave function are separated, and only the spatial part is treated: this is referred to as stationary states that are described by the time-independent Schrödinger equation. In addition, relativistic effects are either neglected or treated within the pseudopotential approach. A further simplification of the problem was introduced by Born and Oppenheimer in 1927 [143], who suggested that, since the electrons move much faster than the nuclei, the latter can be regarded as fixed while the electrons carry out their motions.
Applying the aforementioned approximations, the problem reduces to solving the non-relativistic, time-independent, electronic Schrödinger equation:

$$\hat{H}^{\mathrm{el}}\Psi^{\mathrm{el}} = E^{\mathrm{el}}\Psi^{\mathrm{el}}, \tag{2.2}$$

where $\hat{H}^{\mathrm{el}}$ is the electronic Hamiltonian that acts on the electronic wave function Ψ^{el} to give the electronic energy E^{el}, and it takes the form, in atomic units:

$$\hat{H}^{\mathrm{el}} = -\frac{1}{2}\sum_{i=1}^{N}\nabla_i^2 - \sum_{i=1}^{N}\sum_{A=1}^{M}\frac{Z_A}{r_{iA}} + \sum_{i=1}^{N}\sum_{j>i}^{N}\frac{1}{r_{ij}}. \tag{2.3}$$

The first term in Eq. 2.3 describes the kinetic energy of the electrons and the other two terms denote the electrostatic interaction between electrons and nuclei and among electrons

respectively. N is the number of electrons, M is the number of nuclei, r_{ij} is the distance between electrons i and j and r_{iA} is the distance between electron i and nucleus A.
In this work, the electronic Schrödinger equation is considered and thus, for simplicity, the indices "el" are removed.

2.1 Hartree Fock

Although the aforementioned approximations are frequently used in quantum chemical calculations, the electron-electron repulsion term remains an obstacle for a direct solution of the Schrödinger equation. In the Hartree-Fock scheme [144], the N-electron wave function is approximated by an antisymmetrized product of N one-electron wave functions $\chi_i(x_i)$ that obeys the Pauli exclusion principle. This product is usually referred to as a Slater determinant [145]

$$\Psi(x_1, x_2, ..., x_N) = \frac{1}{\sqrt{N!}} \begin{vmatrix} \chi_1(x_1) & \chi_2(x_1) & \cdots & \chi_n(x_1) \\ \chi_1(x_2) & \chi_2(x_2) & \cdots & \chi_n(x_2) \\ \vdots & \vdots & \ddots & \vdots \\ \chi_1(x_N) & \chi_2(x_N) & \cdots & \chi_N(x_N) \end{vmatrix} \tag{2.4}$$

The one-electron functions $\chi_i(x_i)$ are called spin orbitals and are composed of a spatial orbital $\psi_i(\vec{r})$ and one of the two spin functions, $\alpha(s)$ or $\beta(s)$.

$$\chi_i(x) = \psi_i(\vec{r}) \begin{cases} \alpha(s) \\ \beta(s) \end{cases} \tag{2.5}$$

Following the variational principle, the best Slater determinant Ψ_{HF} is the one that yields the lowest energy and this is expressed as

$$E_0 \leq E_{\mathrm{HF}} = \langle \Psi_{\mathrm{HF}} | \hat{H} | \Psi_{\mathrm{HF}} \rangle = \min_{\Psi} \langle \Psi | \hat{H} | \Psi \rangle, \tag{2.6}$$

where Ψ is a trial wave function that gives the ground state energy E_0.
The differential equations for finding the optimal spin orbitals are called the Hartree-Fock equations [146, 147] and take the form

$$\hat{f} | \chi_i \rangle = \epsilon_i | \chi_i \rangle, \tag{2.7}$$

where ϵ_i are the eigenvalues of the Fock operator $\hat{f}$ and have the physical interpretation of orbital energies. The Fock operator $\hat{f}$ is an effective one-electron operator defined as

$$\hat{f} = -\frac{1}{2}\nabla_i^2 - \sum_{A=1}^{M} \frac{Z_A}{r_{iA}} + \nu^{\mathrm{HF}}(x_i). \tag{2.8}$$

The so-called effective Hartree-Fock potential $\nu^{\mathrm{HF}}(x_i)$ is the average repulsive potential experienced by electron i due to the remaining *N-1* electrons. It has explicitly the two components:

$$\nu^{\mathrm{HF}}(x_i) = \sum_b (\hat{J}_b(x_i) - \hat{K}_b(x_i)). \tag{2.9}$$

The first term in Eq. 2.9 is the Coulomb operator which represents the potential that the electron i in spin orbital χ_a experiences due to the average charge distribution of another electron in spin orbital χ_b. When operating on a spin orbital $\chi_a(x_1)$, it is defined by

$$\hat{J}_b(x_1)\chi_a(x_1) = \int \chi_b^*(x_2)\frac{1}{r_{12}}\chi_b(x_2)dx_2\chi_a(x_1). \tag{2.10}$$

The second term is the exchange contribution to the HF potential. The exchange operator $\hat{K}$ acting on a spin orbital $\chi_a(x_1)$ is expressed as

$$\hat{K}_b(x_1)\chi_a(x_1) = \int \chi_b^*(x_2)\frac{1}{r_{12}}\chi_a(x_2)dx_2\chi_b(x_1). \tag{2.11}$$

Since the Fock operator depends through the HF potential on the spin orbitals, Eq. 2.7 is not a regular eigenvalue equation that can be solved in a closed form. Rather, it has to be solved iteratively, using the so-called self-consistent field (SCF) procedure [148]. In brief, this technique consists of starting with a "guessed" set of spin orbitals, which are used to solve the HF equations. The resulting new set of orbitals is then used in the next iteration and so on until convergence and self-consistency are achieved.
The Hartree-Fock SCF problem is usually solved through the introduction of a finite set of atomic orbitals to expand the unknown molecular orbitals:

$$\psi_i(\vec{r}) = \sum_{\mu=1}^{K} C_{\mu i}\phi_\mu(\vec{r}), \tag{2.12}$$

with the coefficients $C_{\mu i}$ being the only unknowns. The result of this linear expansion is a matrix equation, known as the Roothan-Hall equation [149, 150]

$$\mathbf{FC} = \varepsilon\mathbf{SC}, \tag{2.13}$$

where C is a square matrix containing the expansion coefficients and ϵ is a diagonal matrix of the orbital energies. S is the overlap matrix and F is the Fock matrix, which are hermitian matrices with their elements defined as:

$$S_{\mu\nu} = \int \phi_\mu^*(r_1)\phi_\nu(r_1)\mathrm{dr}_1, \tag{2.14}$$

$$F_{\mu\nu} = \int \phi_\mu^*(\mathrm{r}_1)f(\mathrm{r}_1)\phi_\nu(\mathrm{r}_1)\mathrm{dr}_1. \tag{2.15}$$

2.2 Correlation energy

As seen in the previous section, the Hartree Fock theory is a successful approximation in many cases since it reduces the many-body wave function problem to a set of one-body wave function and therefore minimizes the computational effort. However, the Hartree-Fock SCF wave function treats the interactions between electrons only in an average way and does not take into account the instantaneous interactions between electrons. The energy contribution due to the correlated motions of the electrons is crucial in some cases, where high accuracy is required. It is called correlation energy and is defined as the difference between the nonrelativistic exact energy E_{nonrel} and the Hartree-Fock energy E_{HF}

$$E_{\text{corr}} = E_{\text{nonrel}} - E_{\text{HF}}. \tag{2.16}$$

A variety of computational schemes to determine the correlation contributions accurately and efficiently has been devised during the years. Most of them rely on the HF results and are thus known as post-HF methods.

2.2.1 The CI wave function

A conceptually simple, but computationally demanding approach is the configuration interaction (CI) which, in principle, provides an exact solution of the many-electron problem [114]. The basic idea of this method is to expand the exact wave function in a linear combination of N-electron trial functions (Slater determinants) and use the variational principle to find the expansion coefficients. This allows the calculation of the exact energies of the ground and excited states within the Born-Oppenheimer approximation. If all possible excited determinants are considered, we talk about a full CI calculation and the exact many-electron wave function takes the form:

$$|\Phi\rangle = c_0|\Psi_0\rangle + \sum_{ar} c_a^r|\Psi_a^r\rangle + \sum_{\substack{a<b\\r<s}} c_{ab}^{rs}|\Psi_{ab}^{rs}\rangle + \sum_{\substack{a<b<c\\r<s<t}} c_{abc}^{rst}|\Psi_{abc}^{rst}\rangle + \cdots, \tag{2.17}$$

where *a, b, c, ...* refer to the occupied and *r, s, t, ...* to the unoccupied spin orbitals. Ψ_0 is the HF ground state Slater determinant and Ψ_a^r, Ψ_{ab}^{rs} and Ψ_{abc}^{rst} define a singly, doubly and triply excited determinants, respectively.
Another approach which deals with the electron correlation is the perturbation theory which was applied in this work and will be discussed in detail in the next section.

2.2.2 Perturbation theory

Rayleigh and Schrödinger [151] established an approach in which they introduced a perturbation term to the Hamiltonian. In this approach, the total Hamiltonian is composed of two parts: a zeroth-order part for which we know the eigenfunctions and eigenvalues, and a perturbation part. In the following, we derive the energy expressions of Rayleigh-Schrödinger (RS) perturbation theory following the procedure by Szabo and Ostlund [114].

The eigenvalue problem we wish to solve is expressed by

$$\hat{H}|\Phi_i\rangle = (\hat{H}_0 + \lambda\hat{H}')|\Phi_i\rangle = E_i|\Phi_i\rangle, \tag{2.18}$$

where $\hat{H}_0$ is the unperturbed Hamiltonian of known eigenfunctions $\Phi_i^{(0)}$ and eigenvalues $E_i^{(0)}$, $\hat{H}'$ is the perturbed Hamiltonian and λ is an ordering parameter which controls the order of the perturbation.
The eigenfunctions and the eigenvalues of Eq. 2.18 are expanded in power series in λ:

$$\Phi_i = \Phi_i^{(0)} + \lambda\Phi_i^{(1)} + \lambda^2\Phi_i^{(2)} + \cdots, \tag{2.19}$$

$$E_i = E_i^{(0)} + \lambda E_i^{(1)} + \lambda^2 E_i^{(2)} + \cdots. \tag{2.20}$$

The wave function of $\hat{H}_0$ is considered to be normalized ($\langle\Phi_i^{(0)}|\Phi_i^{(0)}\rangle = 1$), and the wave function of the total Hamiltonian $\hat{H}$ must obey the intermediate normalization such as:

$$\langle\Phi_i^{(0)}|\Phi_i\rangle = 1. \tag{2.21}$$

Substituting Eq. 2.19 into Eq. 2.21 gives:

$$\langle\Phi_i^{(0)}|\Phi_i^{(0)}\rangle + \lambda\langle\Phi_i^{(0)}|\Phi_i^{(1)}\rangle + \lambda^2\langle\Phi_i^{(0)}|\Phi_i^{(2)}\rangle + \cdots = 1. \tag{2.22}$$

Eq. 2.22 holds for all values of λ, therefore:

$$\langle\Phi_i^{(0)}|\Phi_i^{(1)}\rangle = 0, \langle\Phi_i^{(0)}|\Phi_i^{(2)}\rangle = 0, \cdots \tag{2.23}$$

Substitution of equations 2.19 and 2.20 into Eq. 2.18 results in:

$$\begin{aligned}(\hat{H}_0 + \lambda\hat{H}')(|\Phi_i^{(0)}\rangle + \lambda|\Phi_i^{(1)}\rangle + \lambda^2|\Phi_i^{(2)}\rangle + \cdots) = \\ (E_i^{(0)} + \lambda E_i^{(1)} + \lambda^2 E_i^{(2)} + \cdots)(|\Phi_i^{(0)}\rangle + \lambda|\Phi_i^{(1)}\rangle + \lambda^2|\Phi_i^{(2)}\rangle + \cdots).\end{aligned} \tag{2.24}$$

Equating coefficients of λ^n, we have:

$$\hat{H}_0|\Phi_i^{(0)}\rangle = E_i^{(0)}|\Phi_i^{(0)}\rangle, \tag{2.25}$$

$$\hat{H}_0|\Phi_i^{(1)}\rangle + \hat{H}'|\Phi_i^{(0)}\rangle = E_i^{(0)}|\Phi_i^{(1)}\rangle + E_i^{(1)}|\Phi_i^{(0)}\rangle, \tag{2.26}$$

$$\hat{H}_0|\Phi_i^{(2)}\rangle + \hat{H}'|\Phi_i^{(1)}\rangle = E_i^{(0)}|\Phi_i^{(2)}\rangle + E_i^{(1)}|\Phi_i^{(1)}\rangle + E_i^{(2)}|\Phi_i^{(0)}\rangle \tag{2.27}$$

Using the orthogonality relation (Eq. 2.23) and multiplying each of the above equations by $\langle\Phi_i^0|$, the following expressions of the n-th order energies are obtained:

$$E_i^{(0)} = \langle\Phi_i^{(0)}|\hat{H}_0|\Phi_i^{(0)}\rangle \tag{2.28}$$

$$E_i^{(1)} = \langle\Phi_i^{(0)}|\hat{H}'|\Phi_i^{(0)}\rangle \tag{2.29}$$

$$E_i^{(2)} = \langle\Phi_i^{(0)}|\hat{H}'|\Phi_i^{(1)}\rangle \tag{2.30}$$

To determine the second-order correction of the energy $E_i^{(2)}$, the first-order corrected wave function $|\Phi_i^{(1)}\rangle$ is expanded in terms of the eigenfunctions of $\hat{H}_0$:

$$|\Phi_i^{(1)}\rangle = \sum_n c_n |\Phi_n^{(0)}\rangle \tag{2.31}$$

with $c_n = \langle\Phi_n^{(0)}|\Phi_i^{(1)}\rangle$ and $c_i = 0$. Multiplying Eq. 2.26 by $\langle\Phi_n^{(0)}|$ and taking into account the orthogonality of the zeroth-order wave functions, we get for $n \neq i$:

$$(E_i^{(0)} - E_n^{(0)})\langle\Phi_n^{(0)}|\Phi_i^{(1)}\rangle = \langle\Phi_n^{(0)}|\hat{H}'|\Phi_i^{(0)}\rangle, \tag{2.32}$$

hence $|\Phi_i^{(1)}\rangle$ is expressed as:

$$|\Phi_i^{(1)}\rangle = \sum_{n\neq i} \frac{\langle\Phi_n^{(0)}|\hat{H}'|\Phi_i^{(0)}\rangle}{E_i^{(0)} - E_n^{(0)}} |\Phi_n^{(0)}\rangle \tag{2.33}$$

Therefore, substituting Eq. 2.33 into Eq. 2.30 results in the desired expression of the second-order energy:

$$E_i^{(2)} = \sum_{n\neq i} \frac{|\ \langle\Phi_n^{(0)}|\hat{H}'|\Phi_i^{(0)}\rangle\ |^2}{E_i^{(0)} - E_n^{(0)}} \tag{2.34}$$

The correlation energy can be obtained using RS perturbation theory, where $\hat{H}_0$ is the Hartree-Fock Hamiltonian:

$$\hat{H}_0 = \sum_i f(i), \tag{2.35}$$

and the electron correlation represents the perturbation part:

$$\hat{H}' = \sum_{ij} \frac{1}{r_{ij}} - \sum_i \nu^{\mathrm{HF}}(i) \tag{2.36}$$

This improvement of the HF theory is known as Møller-Plesset (MP) perturbation theory [116]. The Hartree-Fock energy is the sum of the zeroth and first-order perturbation energies:

$$E_0 = E_0^{(0)} + E_0^{(1)} = \sum_a \varepsilon_a + \langle\Phi^{(0)}|\sum_{i<j} \frac{1}{r_{ij}}|\Phi^{(0)}\rangle - \langle\Phi^{(0)}|\sum_i \nu^{\mathrm{HF}}(i)|\Phi^{(0)}\rangle \tag{2.37}$$

Therefore, second-order perturbation theory is applied to determine the electron correlation. The second-order energy required in MP theory is derived from Eq. 2.34 and is expressed as:

$$E_0^{(2)} = \sum_{\substack{a<b \\ r<s}} \frac{|\ \langle ab|rs\rangle - \langle ab|sr\rangle\ |^2}{\varepsilon_a + \varepsilon_b - \varepsilon_r - \varepsilon_s} \tag{2.38}$$

where a and b represent the occupied spin orbitals, r and s represent the virtual spin orbitals and $\varepsilon_a, \varepsilon_b, \varepsilon_r$ and ε_s are the orbital energies.

2.3 Density functional theory

2.3.1 The Hohenberg-Kohn theorems

Density functional theory (DFT) constitutes a powerful tool for predicting the ground state properties of a system, with the electron density being the key quantity. It dates back to the work of Thomas and Fermi in 1927, who applied a quantum statistical model on the electron density [152, 153]. However, DFT became a vastly popular theory only from the time that Hohenberg and Kohn established their two theorems in 1964 [154].
The electron density represents the probability of finding an electron within the volume element $d\overrightarrow{r_1}$ but with arbitrary spin and it is defined as:

$$\rho(\overrightarrow{r_1}) = N \int \cdots \int |\Psi(x_1, x_2, \cdots, x_N)|^2 ds_1 dx_2 \cdots dx_N. \tag{2.39}$$

In the first Hohenberg-Kohn theorem, the electron density $\rho(\overrightarrow{r})$ defines an external potential uniquely up to a constant. This implies that the ground state energy is a functional of the ground state electron density and it can be written as

$$E[\rho] = E_{\text{ne}}[\rho] + T[\rho] + E_{\text{ee}}[\rho] \tag{2.40}$$

E_{ne} defines the potential energy due to the nuclei-electron attraction and it can be expressed through the external potential from the nuclei as:

$$E_{\text{ne}}[\rho] = \int \rho(\vec{r}) \nu_{\text{ext}}(\vec{r}) d\vec{r} \tag{2.41}$$

T is the kinetic energy of the electrons and E_{ee} the electron-electron repulsion.
The second Hohenberg-Kohn theorem states that the energy obtained from the functional expressed in Eq. 2.40 is higher for any trial density ρ_t than the true ground state energy E_0.

$$E_0 \leq E[\rho_t] \tag{2.42}$$

In this theorem, the variational principle is applied on the electron density.
Using the Hohenberg-Kohn theorems, we are in principle able to determine the ground state energy of the system. However, the major challenge remains to find explicit expressions for the two functionals $T[\rho]$ and $E_{\text{ee}}[\rho]$ given in Eq. 2.40.

2.3.2 The Kohn-Sham approach

The concept introduced by Kohn and Sham [155], a year after the contribution of Hohenberg and Kohn, marked the real breakthrough in modern DFT. Their approach considers a system of non-interacting electrons described by a set of orbitals $\phi_i(\vec{r})$ whose resulting density is exactly equal to the density of the interacting system:

$$\rho(\vec{r}) = \sum_i^N \phi_i^2(\vec{r}) = \rho_0(\vec{r}). \tag{2.43}$$

The Hamiltonian of the non-interacting system includes an effective potential $\nu_{\text{eff}}(\vec{r})$:

$$\hat{H}^{\text{KS}} = -\frac{1}{2}\sum_{i=1}^{N}\nabla_i^2 + \sum_{i=1}^{N}\nu_{\text{eff}}(\vec{r}), \tag{2.44}$$

and its exact wave function is represented by a Slater determinant of the Kohn-Sham spin orbitals $\phi_i(r)$ which are solutions of the Kohn-Sham equation:

$$\hat{f}^{\text{KS}}\phi_i(\vec{r}) = (-\frac{1}{2}\nabla_i^2 + \nu_{\text{eff}}(\vec{r}))\phi_i(\vec{r}) = \varepsilon_i\phi_i(\vec{r}). \tag{2.45}$$

The electronic energy of the real interacting system is expressed as:

$$\begin{aligned} E[\rho] &= E_{\text{ne}}[\rho] + T_{\text{s}}[\rho] + J[\rho] + E_{\text{XC}}[\rho] \\ &= \int \rho(\vec{r})\nu_{\text{ext}}(\vec{r})\text{d}\vec{r} + T_{\text{s}}[\rho] + \frac{1}{2}\iint \frac{\rho(\vec{r}_1)\rho(\vec{r}_2)}{\vec{r}_{12}}\text{d}\vec{r}_1\text{d}\vec{r}_2 + E_{\text{XC}}[\rho], \end{aligned} \tag{2.46}$$

where $T_{\text{s}}[\rho]$ is the kinetic energy of the non-interacting system, $J[\rho]$ is the classical electrostatic energy between two densities $\rho(\vec{r}_1)$ and $\rho(\vec{r}_2)$ and $E_{\text{XC}}[\rho]$ is the so-called exchange-correlation energy defined as:

$$E_{\text{XC}}[\rho] = (T[\rho] - T_{\text{S}}[\rho]) + (E_{\text{ee}}[\rho] - J[\rho]) = T_{\text{C}}[\rho] + E_{\text{ncl}}[\rho] \tag{2.47}$$

A part of $E_{\text{XC}}[\rho]$ is $T_{\text{C}}[\rho]$, the difference between the true kinetic energy $T[\rho]$ and the kinetic energy of the non-interacting system $T_{\text{S}}[\rho]$. The term $E_{\text{ncl}}[\rho]$ refers to the non-classical electrostatic contributions comprising the effects of self-interaction correction, exchange and correlation.
The kinetic energy of the non-interacting reference system can be expressed as:

$$T_{\text{S}} = -\frac{1}{2}\sum_{i}^{N}\langle\phi_i|\nabla^2|\phi_i\rangle. \tag{2.48}$$

Using Eq. 2.48 and the dependence on the orbitals shown in Eq. 2.43, the expression of the electronic energy becomes:

$$\begin{aligned} E[\rho] = &-\sum_{i}^{N}\int\sum_{A}^{M}\frac{Z_A}{r_{1A}}|\phi_i(\vec{r}_1)|^2 d\vec{r}_1 - \frac{1}{2}\sum_{i}^{N}\langle\phi_i|\nabla^2|\phi_i\rangle + \\ &\frac{1}{2}\sum_{i}^{N}\sum_{j}^{N}\iint|\phi_i(\vec{r}_1)|^2\frac{1}{r_{12}}|\phi_j(\vec{r}_2)|^2 d\vec{r}_1 d\vec{r}_2 + E_{\text{XC}}[\rho]. \end{aligned} \tag{2.49}$$

In principle, the Kohn-Sham approach is exact and Eq. 2.49 would lead to the exact energy if an explicit form of the exchange-correlation energy $E_{\text{XC}}[\rho]$ was known. Unfortunately, it is not the case and approximations have to be introduced in applications.

2.3.3 Exchange-correlation functionals

The first approximation to the exchange-correlation functional is the so-called local density approximation (LDA) [156–158] which represents the bedrock of almost all further approximations. This approach is based on the uniform electron gas model, in which "electrons are considered to move on a positive background charge distribution such that the total ensemble is electrically neutral". The assumption followed in the LDA is to write E_{XC} in the following form:

$$E_{\mathrm{XC}}^{\mathrm{LDA}}[\rho] = \int \rho(\mathrm{r})\varepsilon_{\mathrm{XC}}[\rho]\mathrm{d}\vec{r}, \tag{2.50}$$

where $\varepsilon_{\mathrm{XC}}[\rho]$ represents the exchange-correlation energy per particle of the homogeneous electron gas and it can be further written as the sum of the exchange and correlation contributions:

$$\varepsilon_{\mathrm{XC}}[\rho] = \varepsilon_{\mathrm{X}}[\rho] + \varepsilon_{\mathrm{C}}[\rho]. \tag{2.51}$$

While the exchange part can be analytically calculated through the Slater exchange functional, there exist no explicit expression for the correlation part. However, it has been provided by Ceperley and Alder [159] highly accurate quantum Monte Carlo simulations, which were later used by Vosko, Wilk and Nusair in interpolation schemes to develop analytical expressions of ε_{C}, generating the most widely used correlation functional VWN [158]. Unfortunately, LDA is not the best choice for most applications in chemistry since it does not account for the inhomogeneity effects of the electron density on exchange and correlation. Therefore, the generalized gradient approximation (GGA) was applied to improve on LDA. In a GGA functional, a dependence on the gradients of the electron density is added and the expression of the exchange-correlation functional becomes:

$$E_{\mathrm{XC}}^{\mathrm{GGA}}[\rho] = \int \rho(\vec{r})\varepsilon_{\mathrm{XC}}[\rho, \nabla\rho]\mathrm{d}\vec{r}. \tag{2.52}$$

A variety of GGA functionals has been put forward, some of which are based on semi-empirical parameters such as the PW91 functional [160], while others are derived from first principles like the implementation of Perdew, Burke and Ernzerhof (PBE) [161].
A more recent approach to deal with the exchange-correlation functional is offered by the hybrid functionals in which the exact Hartree-Fock exchange is mixed with LDA and GGA exchange functionals; the correlation part is defined by mixing LDA and GGA correlation. The most widely used hybrid functional is B3LYP which mixes exact exchange $E_{\mathrm{X}}^{\mathrm{exact}}$ with exchange from LDA and the Becke 88 functional [162], and combines the VWN correlation functional with the GGA functional by Lee, Yang and Parr [163] according to the following equation:

$$E_{\mathrm{XC}}^{\mathrm{B3LYP}} = (1-a-b)E_{\mathrm{X}}^{\mathrm{Dirac}} + aE_{\mathrm{X}}^{\mathrm{HF}} + bE_{\mathrm{X}}^{\mathrm{B88}} + (1-c)E_{\mathrm{C}}^{\mathrm{VWN}} + cE_{\mathrm{C}}^{\mathrm{LYP}} \tag{2.53}$$

with the parameter values $a = 0.20$, $b = 0.72$ and $c = 0.81$ giving good fits to experimental molecular atomization energies. B3LYP has been applied in this thesis, in addition to the earlier hybrid functional B3PW which treats the exchange contribution like in the case of

B3LYP but mixes VWN correlation with the PW91 functional [164] to describe the correlation part.

2.3.4 Dispersion correction for DFT

Electron correlation effects are known to be responsible of the so-called dispersion interactions, which are the attractive interactions arising from quantum-induced instantaneous multipoles in molecules. The former constitute a part of the van der Waals forces which include also the electrostatic and induction interactions.
The London dispersion interaction between two species A and B can be expressed as:

$$E_{\text{disp}} \approx -\frac{3I_p^A I_p^B}{2(I_p^A + I_p^B)} \frac{\alpha^A \alpha^B}{r^6} \tag{2.54}$$

where I_p^A , I_p^B denote the ionization energies and α^A , α^B the polarizabilities of species A and B.
Dispersion interactions play a significant role in understanding the chemistry of large systems and therefore inclusion of these interactions in chemical calculations leads to high accurate results. Despite the fact that density functional theory has become the method of choice for electronic structure calculations, standard density functionals usually fail to describe the long-range dispersion interactions correctly. A dispersion correction to the conventional density functionals was initially proposed by Yang [165] and later developped by Grimme [108]. This approach, usually termed as DFT-D, is based on an atom pairwise additive treatment of the dispersion energy and it is known with many different variants.
The DFT-D2 approach adds a semi-empirical dispersion potential to the Kohn-Sham DFT energy, taking the following explicit form:

$$E_{\text{disp}}^{\text{D2}} = -s_6 \sum_{i=1}^{n-1} \sum_{j=i+1}^{n} \frac{C_{ij}^{[6]}}{r_{ij}^6} f_{\text{dmp}}(r_{ij}) \tag{2.55}$$

In this modification, the dispersion coefficients $C_{ij}^{[6]}$ are summed over interatomic distances r_{ij}, modulated by a damping function $f_{\text{dmp}}(r_{ij})$ that determines the range of the dispersion correction. s_6 is a global scaling factor that is optimized to be unique to each density functional.
A refined modification, named as DFT-D3 [109], was presented by Grimme in 2010 seeking to improve on the accuracy of DFT-D2 and including less empiricism. Here, an additional r^{-8} term, as well as three-body terms, are incorporated in the dispersion energy and the $C_{ij}^{[6]}$ coefficients are adjusted such that they become environment dependent. The three-body dispersion contribution calculated with D3 is expressed as:

$$E^{(3)} = \sum_{\text{ABC}} f_{\text{dmp}}(\bar{r}_{\text{ABC}}) \frac{C_{\text{ABC}}^{[9]} (3 \cos\theta_a \cos\theta_b \cos\theta_c + 1)}{(r_{\text{AB}} r_{\text{BC}} r_{\text{CA}})^3}, \tag{2.56}$$

where θ_a, θ_b and θ_c represent the angles of the triangle formed by r_{AB}, r_{BC} and r_{CA}, the geometrical mean of which is expressed by $\bar{r}_{\mathrm{ABC}}$. The $C^{[9]}$ coefficient is approximated by applying the geometric average of the two-body coefficients $C^{[6]}$:

$$C^{[9]}_{\mathrm{ABC}} = -\sqrt{C^{[6]}_{\mathrm{AB}} C^{[6]}_{\mathrm{BC}} C^{[6]}_{\mathrm{CA}}}. \tag{2.57}$$

In order to avoid near singularities for small distances, the use of damping functions is crucial. Several varieties of damping exist, including the zero-damping:

$$f^{\mathrm{D3(0)}}_{\mathrm{dmp,n}}(r_{ij}) = \left[1 + 6\left(\frac{r_{ij}}{s_{r,n} r_{0,ij}}\right)^{-\alpha_n}\right]^{-1}, \tag{2.58}$$

and the so-called Becke-Johnson damping which is the generally preferred style of DFT-D3 and takes the form:

$$f^{\mathrm{D3(BJ)}}_{\mathrm{dmp,n}}(r_{ij}) = \frac{r^n_{ij}}{r^n_{ij} + (\alpha_1 r_{0,ij} + \alpha_2)^n}. \tag{2.59}$$

2.4 Crystalline solids and periodic boundary conditions

2.4.1 The Schrödinger equation for solids

A crystalline solid is defined as an infinite periodic arrangement of atoms in three-dimensional space generated by a set of translation vectors

$$\vec{\mathbf{T}} = n_1 \vec{\mathbf{a}}_1 + n_2 \vec{\mathbf{a}}_2 + n_3 \vec{\mathbf{a}}_3 \tag{2.60}$$

where $\mathbf{a}_i$ are the basis vectors that characterize a primitive unit cell and n_{i} are integer numbers including zero. In other words, crystalline systems feature a translational symmetry that corresponds to the set of vectors $\vec{\mathbf{T}}$ defining the so-called direct lattice. Besides the latter, it is crucial to consider also the reciprocal lattice in the study of periodic systems. In reciprocal space, a crystalline solid is characterized by the reciprocal lattice vector $\vec{\mathbf{K}}$ which is expressed, like in the case of direct lattice, as a linear combination of reciprocal lattice basis vectors $\vec{\mathbf{b}}_i$:

$$\vec{\mathbf{K}} = m_1 \vec{\mathbf{b}}_1 + m_2 \vec{\mathbf{b}}_2 + m_3 \vec{\mathbf{b}}_3 \tag{2.61}$$

m_1, m_2 and m_3 are integer values that represent a family of lattice planes orthogonal to each reciprocal vector $\vec{\mathbf{k}}$ with integers m_1, m_2, m_3, and they are denoted by the so-called Miller indices [166]. The reciprocal lattice basis vectors $\vec{\mathbf{b}}_i$ are related to the direct lattice basis vectors $\vec{\mathbf{a}}_i$ by:

$$\vec{\mathbf{a}}_i \vec{\mathbf{b}}_j = 2\pi \delta_{ij} \tag{2.62}$$

The reciprocal lattice vectors should obey

$$e^{i\vec{\mathbf{K}}\cdot\vec{\mathbf{T}}} = 1 \tag{2.63}$$

showing that two vectors $\vec{\mathbf{k}}$ and $\vec{\mathbf{k}}'$ are equivalent if they differ only by a lattice vector $\vec{\mathbf{K}}$. Therefore, for the description of a crystalline system, only $\vec{\mathbf{k}}$-vectors within a restricted region, known as the first Brillouin zone [167], have to be considered.
As a general consequence of translation symmetry of the crystals, Bloch's theorem [168] is applied:

$$\hat{T}\Phi(\vec{\mathbf{r}},\vec{\mathbf{k}}) = \Phi(\vec{\mathbf{r}}+\vec{\mathbf{T}},\vec{\mathbf{k}}) = e^{i\vec{\mathbf{k}}\cdot\vec{\mathbf{T}}}\Phi(\vec{\mathbf{r}},\vec{\mathbf{k}}) \tag{2.64}$$

where $\hat{T}$ is a translation operator that corresponds to the direct lattice vector $\vec{\mathbf{T}}$. The eigenfunctions of the crystal Hamiltonian $\Phi(\vec{\mathbf{r}},\vec{\mathbf{k}})$ are called Bloch functions and they can be written as the product of a plane wave of vector $\vec{\mathbf{k}}$ within the first Brillouin zone and a periodic function u having the same periodicity of the direct lattice:

$$\Phi(\vec{\mathbf{r}},\vec{\mathbf{k}}) = e^{i\vec{\mathbf{k}}\cdot\vec{\mathbf{r}}}u(\vec{\mathbf{r}},\vec{\mathbf{k}}) \tag{2.65}$$

To solve the Schrödinger equation of crystalline systems, the periodic boundary conditions and the self-consistent field approximation discussed in section 2.1 are employed. The single-particle wave functions, called crystalline wave functions, are expressed as linear combinations of Bloch functions [169–172]:

$$\psi_i(\vec{\mathbf{r}},\vec{\mathbf{k}}) = \sum_{\mu} c_{\mu i}(\vec{\mathbf{k}})\Phi(\vec{\mathbf{r}},\vec{\mathbf{k}}) \tag{2.66}$$

where $c_{\mu i}(\vec{\mathbf{k}})$ represent the coefficients which can be calculated by solving iteratively the coupled set of matrix equations in a similar procedure as that for non-periodic systems:

$$F(\vec{\mathbf{k}})C(\vec{\mathbf{k}}) = S(\vec{\mathbf{k}})C(\vec{\mathbf{k}})E(\vec{\mathbf{k}}) \tag{2.67}$$

Bloch functions are in turn expanded in a set of basis functions, following two different approaches that are both implemented in quantum chemical codes for periodic systems. The first type of basis functions, referred to as plane waves, is a symmetry-adapted wave function satisfying the periodic boundary conditions. This type is the natural choice for periodic functions. However, a high number of plane waves is required for the description of the wave function in the core region [173].
The other type is called atomic orbitals, which have the advantage of a consistent description of valence and core electrons. The Bloch functions are here constructed from the linear combination of these orbitals (LCAO) as [174]:

$$\Phi_i(\vec{\mathbf{r}},\vec{\mathbf{k}}) = \frac{1}{\sqrt{N}}\sum_{\vec{\mathbf{T}}} e^{i\vec{\mathbf{k}}\cdot\vec{\mathbf{T}}}\phi_i(\vec{\mathbf{r}}-\vec{\mathbf{r}}_A-\vec{\mathbf{T}}) \tag{2.68}$$

with N the normalization, i the atomic orbital in the unit cell and ϕ_i an atomic orbital centered in the atomic position $\mathbf{r}_A$ of the reference cell. Atomic orbitals have the advantage of an accurate description of core and valence electrons, and an effective use in correlation methods through the localization of Bloch functions formed from these orbitals. In this

work, I applied the LCAO approach for the DFT and Hartree-Fock calculations using the CRYSTAL09 software package [175, 176].

2.4.2 Local MP2 for periodic systems

The computational cost of electron correlation methods is high and increases dramatically with the size of the system. In the MP2 method, the scaling of the computational effort is $O(N^5)$, where N is the relative measure of the system size. This scaling becomes $O(N^6)$ for MP3 and CCSD, and reaches $O(N^7)$ for MP4 and CCSD(T). Such high costs prohibit the use of these canonical correlation methods for the calculation of large systems. For the sake of reducing the computational cost, canonical orbitals are replaced by localized orbitals, following a unitary localization procedure [177]. The local MP2 method originally proposed by Saebo and Pulay [121–123] is one of the most successful attempts to deal with the high scaling wall of electron-correlation methods. Instead of using Bloch orbitals that extend over the entire crystalline system, localized molecular orbitals (LMOs) within a certain spatial region are employed to span the occupied manifold. The virtual space is well-localized and truncated into an excitation domain, where only virtual orbitals lying in a spatial vicinity of the corresponding occupied ones are considered. In the last few years, the LMP2 approach was combined with integral-direct techniques leading to a linear scaling of the computational effort [178].
The periodic local MP2 scheme [126, 128] is applied for the calculation of adsorption energies throughout this work, as implemented in the CRYSCOR code [127, 128]. The latter is based on the localized crystalline orbitals which are obtained from the localization of the canonical Bloch functions produced by CRYSTAL [179, 180], following the Boys localization procedure [179, 181]. These orbitals are called Wannier functions [182] and are used to span the occupied space. The virtual space is described with a set of nonorthogonal local functions, referred to as projected atomic orbitals, which are generated by projecting out the occupied space directly from the atomic orbitals, keeping their orthogonality to the Wannier functions [121].
The MP2 energy per unit cell is expressed as:

$$E_{\mathbf{ij}}^{\mathrm{LMP2}} = \sum_{\mathbf{a,b\ in[i,j]}} K_{\mathbf{ab}}^{\mathbf{ij}} (2T_{\mathbf{ab}}^{\mathbf{ij}} - T_{\mathbf{ba}}^{\mathbf{ij}}) \tag{2.69}$$

where K denote the electron repulsion integrals and T the corresponding excitation amplitudes. The labels **(i , j)** represent pairs of Wannier functions (WFs), in which Wannier function **i** is in the reference cell while **j** spans in principle the whole space. **(a , b)** are pairs of virtual projected atomic orbitals. Electron pairs are treated hierarchically depending on the minimum distance between the two correlated WFs and are thus classified into strong, weak and distant. The strong and weak pairs are usually treated in CRYSCOR as a unique set, that of close-by pairs, within the periodic density fitting technique [183]. For the treatment of distant pairs, the multipolar approximation [184] is used. Very distant pairs are completely neglected.

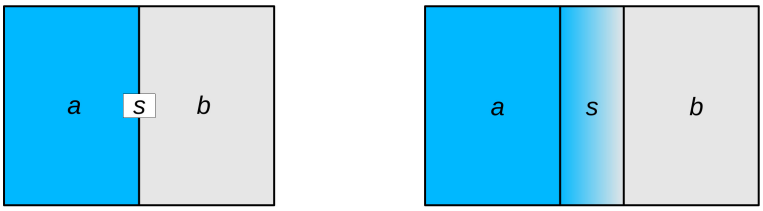

Figure 2.1: Thermodynamic treatment of interfaces. (a) The interface as a boundary separating two homogeneous bulk phases, according to the Gibbs model. (b) The interface as a distinct inhomogeneous phase, according to the Guggenheim model.

2.5 Surface thermodynamics

2.5.1 The surface energy of a solid in gas environment

The spontaneity of processes at constant pressure and temperature is achieved by the minimization of a thermodynamic potential, called the Gibbs energy G [185]. For a closed system, G is defined as:

$$G = U - TS + PV \tag{2.70}$$

with U denoting the internal energy, T the temperature, S the entropy, P the pressure and V the volume.
For an open system composed of different phases j and components i, in which the particles are allowed to exchange between phases, the expression of the change in the Gibbs free energy as function of temperature and pressure is:

$$dG = -\sum_j S^j dT + \sum_j V^j dP + \sum_j \sum_i \mu_i^j dn_i^j. \tag{2.71}$$

where μ_i^j denotes the chemical potential of the chemical component i, and it is consequently expressed as:

$$\mu_i = \left(\frac{\partial G}{\partial n_i}\right)_{P,T}. \tag{2.72}$$

At constant temperature and pressure, Eq. 2.71 becomes:

$$\Big(dG\Big)_{T,P} = \sum_j \sum_i \mu_i^j dn_i^j. \tag{2.73}$$

For a system in thermodynamic equilibrium, the Gibbs free energy is at its minimum, that is $dG = 0$. Applying this condition to a system composed of two phases a and b, it follows that:

$$\sum_i \mu_i^a dn_i^a + \sum_i \mu_i^b dn_i^b = 0. \tag{2.74}$$

The aforementioned discussions concern the bulk phases of a system, and do not deal with

the interface between the phases. The thermodynamics of interfaces can be treated in two different approaches, illustrated in Fig. 2.1. The first one dates back to 1878 and was proposed by Gibbs [186] who regarded the interface as a mathematical surface separating two homogeneous bulk phases. All measurements, according to Gibbs, are referred to a hypothetical reference state consisting of two homogeneous phases meeting at an abrupt dividing surface. The second approach, introduced by Guggenheim [187], treats the interface as a distinct inhomogeneous phase of well-defined volume and material content, the boundaries of which are trapped inside the adjacent bulk phases.
Following the Guggenheim model, the total Gibbs energy of a system composed of two phases a and b separated by an interface phase s is written as:

$$G^{\mathrm{tot}} = G^a + G^s + G^b. \tag{2.75}$$

Since the interface is, according to Guggenheim, a distinct phase of specific area, its Gibbs energy is defined with respect to its area A. Hence, the surface energy γ per area unit is expressed as:

$$\gamma = \frac{1}{A}\left(G^{\mathrm{tot}} - G^a - G^b\right). \tag{2.76}$$

Considering a system composed of a solid in contact with a gas phase. This is regarded as

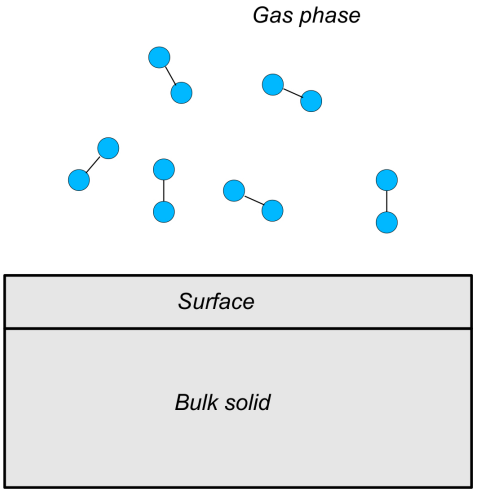

Figure 2.2: Surface in thermodynamic equilibrium with a surrounding gas phase and the underlying bulk phase.

a finite slab which is a part of the infinite solid, and on the surface of the slab are adsorbed the gas molecules (see Fig. 2.2). From a thermodynamic point of view, the system consists of three phases, the bulk solid, the surface and the gas phase, all being in thermodynamic equilibrium. The Gibbs energy of the adsorbates can be expressed through the chemical potential, $G^{\mathrm{ads}} = \sum_i n_i^{\mathrm{ads}} \mu_i^{\mathrm{ads}}$, which implies a temperature and pressure dependence of the adsorbates' Gibbs energy. Therefore, the surface energy is temperature- and pressure-

dependent and is written as:

$$\gamma = \frac{1}{2A}\Big(G^{\text{slab}} - n^{\text{bulk}}\mu^{\text{bulk}} - \sum_i n_i^{\text{ads}}\mu_i^{\text{ads}}\Big). \tag{2.77}$$

G^{slab} is the Gibbs energy of a slab composed of n^{bulk} formula units and μ^{bulk} the Gibbs energy per formula unit in bulk. The factor 1/2 accounts for the fact that the slab is symmetric and has an upper and a lower surfaces.
Up to now, the formalism described is completely based on the Gibbs free energies of the system. Nevertheless, when first principles calculations are combined to surface thermodynamics, the vibrational contributions to the total energy are notably small compared to the electronic energy and are therefore neglected. That allows for employing pure electronic energy values for the solid terms instead of using G^{slab} and G^{bulk}.

2.5.2 Wulff construction

According to the Gibbs thermodynamic principle, a system attains equilibrium by minimizing its Gibbs free energy. If the system consists of two phases in contact with each other, equilibrium is obtained when the free energy of the interface is a minimum. In the case of crystalline solids, a surface is characterized by integer Miller indices and the surface energy depends on its orientation, the ideal shape of the crystal in equilibrium is then determined by the minimal surface energy. These concepts were first discussed by J. W. Gibbs in his fundamental work *"On the Equilibrium of Heterogeneous Substances"* where he shows the role of the anisotropic surface energy in the determination of the shape of a crystal in equilibrium [188]. He also discusses the complexities of crystal growth in large systems. In 1901, G. Wulff reported his results on classical experiments on crystal growth [189] and concluded, after determining the growth rate of different faces, that the surface free energies play a crucial role in the crystal growth progress and in determining the orientation of molecules in the crystals. His findings include the famous Wulff's theorem stating that "the minimum surface energy of a polyhedron at constant volume is reached when the distance of its surfaces from a given point is proportional to the surface tension of these surfaces" [189]. The equilibrium shape of a crystal can be graphically determined following a procedure called *Wulff construction*, as shown in Fig. 2.3. In brief, this is achieved by drawing vectors from a chosen origin with a length proportional to the surface energy. Planes normal to these vectors are then drawn. The inner envelope of these planes forms the ideal shape of the crystal in equilibrium state.

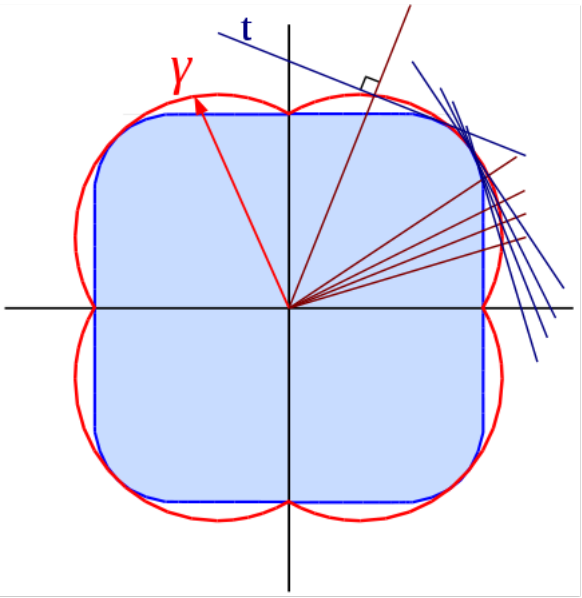

Figure 2.3: Two-dimensional representation of the Wulff construction [190]. The red vector corresponds to a polar plot of the surface energy, the blue lines represent the Wulff planes and the inner envelope in blue corresponds to the equilibrium shape of the crystal.

3 Computational methods and models

The computational parameters and models applied in this work have been introduced in Papers P1-P4. This chapter supplies additional information on some technical details and includes also results for test calculations that are not published. In section 3.1, computational specifications, as an extension to the computational parameters described in the corresponding publications, are discussed. The surface modelling within the periodic scheme is described in section 3.2, including data for the energy convergence with slab thickness. The calculations and approximations required for surface thermodynamics are introduced in section 3.3.

3.1 Computational specifications

If not mentioned otherwise, periodic DFT and HF calculations were performed using the CRYSTAL09/13 [175, 176] quantum chemical package. The latter employs Gaussian-type basis functions localized on atoms for the expansion of the crystalline orbitals. Unfortunately, atomic basis functions suffer from the so-called basis set superposition error (BSSE) [191, 192] which is of importance in solid state calculations. The BSSE arises from the inconsistent treatment of the basis set for a system and its separate components, since the wave function of a component is expanded in much less basis functions than the wave function of the whole system. A possible way to correct for the BSSE is the use of the counterpoise correction (CP) scheme [193], in which the system and the components are described with a basis set of equal size. The correction is then achieved by introducing ghost functions, i.e. basis functions which have neither electrons nor nuclear charges. The CP scheme has been applied in the present work to account for the BSSE.

To reduce the computational effort of the calculations, only valence electrons were treated explicitly while pseudo potentials were used for the description of the core region. The group II metal atoms Ca, Sr and Ba were described by scalar-relativistic energy-consistent pseudopotentials [194] that simulate their inactive [Ne], [Ar]$3d^{10}$ and [Kr]$4d^{10}$ cores, respectively, and a corresponding cc-pVDZ basis set was employed [195]. The Zn atom was described by effective core potential of same quality treating explicitly 20 valence electrons [196], with a corresponding valence triple-zeta basis set augmented by an f polarization function (exponent 3.22) [72].

Periodic local MP2 calculations were performed with the CRYSCOR09 code [127, 128], which employs localized symmetry adapted Wannier functions (WF) for the description of the occupied HF manifold and nonorthogonal projected atomic orbitals for representing the virtual space. First, a HF calculation is performed with CRYSTAL09 [175, 176], followed by a prop-

Table 3.1: Surface energies γ (in J/m^2) for the five low-index surfaces of ZnF_2 at different slab thicknesses.

(hkl)	Nb of ZnF_2 units	Nb of layers	γ
(110)	10	15	0.48
	12	18	0.45
(100)	10	30	0.51
	12	36	0.48
(101)	10	15	0.57
	12	18	0.55
(001)	10	10	0.72
	12	12	0.71
(111)	9	17	0.85
	11	21	0.83

erties calculation which generates localized symmetrized WFs. The latter are then used by a CRYSCOR09 calculation to compute the correlation energy. In the localization step, only valence electrons were considered, adopting the scheme in Refs [179, 197] as implemented in the CRYSTAL09 program.

3.2 The slab model

Surfaces were modelled by slabs that are cut from the three-dimensional bulk crystal along a Miller index plane, in the directions of which the slab is periodic, while it is finite in the direction perpendicular to the surface. Atoms at the surface of the generated slab possess lower coordination compared to the bulk and are therefore accessible for molecules which come into contact with the material. In the search of stoechiometric symmetric slabs yielding a converged surface energy and converged Mulliken charges at a reasonable computational cost, I have tested different terminations and thicknesses of the slabs. The number of atomic layers differ from one slab to another, due to a different composition of the layers. The latter are defined with respect to the z-coordinate: atoms having the same z-coordinate constitute one layer in the slab. The convergence of the surface energy with slab thickness for low-index ZnF_2 surfaces is listed in table 3.1. I used slabs of 10 ZnF_2 units for all surfaces, except for the (111) surface for which 9 ZnF_2 units were used to keep up the symmetry of the slab. For the (001) slab, 10 ZnF_2 units correspond to 10 stoechiometric atomic layers, whereas slab (100) consists of 30 atomic layers with sequence F-Zn-F and slabs (110) and (101) consist of 18 atomic layers with sequences F-(Zn,Zn,F,F)-F and (F,F)-(Zn,Zn)-(F,F), respectively.

The energy convergence with slab thickness has also been tested for MF_2 (M = Ca, Sr

Table 3.2: Surface energies γ (J/m^2) for the three stable surfaces of CaF_2, SrF_2 and BaF_2 at different slab thicknesses.

CaF_2			SrF_2			BaF_2		
(hkl)	Nb of layers	γ	(hkl)	Nb of layers	γ	(hkl)	Nb of layers	γ
(111)	6	0.470	(111)	6	0.451	(111)	6	0.386
	9	0.472		9	0.454		9	0.388
	12	0.472		12	0.454		12	0.388
(110)	5	0.723	(110)	5	0.681	(110)	5	0.572
	6	0.714		6	0.675		6	0.568
	7	0.718		7	0.677		7	0.569
(100)	13	0.944	(100)	13	0.981	(100)	13	0.860
	15	0.955		15	0.984		15	0.859
	17	0.951		17	0.985		17	0.859

and Ba) surfaces, and the results are given in table 3.2. Surface energies were calculated for different numbers of atomic layers in each slab. For the (111) slab, 2 MF_2 units, corresponding to 6 atomic layers, were enough to yield a converged surface energy. Convergence was achieved for 6 and 7 formula units in the case of slabs (110) and (100), respectively. In the former case, the slab consists of 6 atomic layers where each atom constitutes one layer. In the latter case, the slab of 7 MF_2 units corresponds to 15 atomic layers with sequence(F,F)-M-(F,F). Here, a reconstruction was necessary to maintain stoechiometry, and it was done by removing two F^- anions, one from the top and one from the bottom of the slab.

The surface energy of a stoechiometric symmetric slab was calculated as:

$$E^{\text{surf}} = \frac{1}{2A}(E^{\text{slab}} - nE^{\text{bulk}}) \tag{3.1}$$

with n the number of formula units in the slab, E^{slab} the total energy of the relaxed slab, E^{bulk} the total energy per bulk unit cell and A the area of the slab unit cell. The $\frac{1}{2}$ is necessary to account for the upper and the lower surface in a two dimensional slab.

Adsorption was modelled by placing the diatomic molecule above the coordinatively unsaturated surface cations at a distance of about 2.5 Å, relaxing the nuclear coordinates of the slabs and the adsorbates and keeping the lattice constants, already optimized for the bulk, fixed. To model the 50 % and the 25 % coverages, larger surface unit cells were constructed, trying to maximize the distance between the adsorbates. A variety of starting configurations were tested for each adsorption system leading to different minima, and only the most stable structure was considered. Basis set superposition error correction was only applied for the energy at the minimum. For calculating the adsorption energy, several calculations had to be done: first, a structure optimization calculation for the whole periodic system

slab+adsorbant yielding the energy at the minimum $E(\mathrm{s}+\mathrm{ads})$, two single point calculations to evaluate the BSSE corrected energies $E(\mathrm{s}+\mathrm{GF_{ads}})$ of surface and $E(\mathrm{ads}+\mathrm{GF_s})$ of adsorbant layer, at the minimum structure, two single point calculations for the energy of each component (slab or adsorbant) in the adsorption structure but isolated from the other component and two structure optimization calculations for the minimum energy of each free component, the latter four calculations leading to the relaxation energies of the slab $\Delta E_{\mathrm{rel}}\,(\mathrm{s})$ and the adsorbate $\Delta E_{\mathrm{rel}}\,(\mathrm{ads})$. For the latter, the relaxation energy is calculated for one free molecule and multiplied by the number N of adsorbates in the surface unit cell. Hence, the adsorption energy per molecule was obtained as:

$$E_{\mathrm{ads}} = \frac{1}{N}\left[E\,(\mathrm{s}+\mathrm{ads}) - E\,(\mathrm{s}+\mathrm{GF_{ads}}) - E\,(\mathrm{ads}+\mathrm{GF_s}) - \Delta E_{\mathrm{rel}}\,(\mathrm{s}) - \mathrm{N}\Delta\mathrm{E}_{\mathrm{rel}}\,(\mathrm{ads})\right]. \quad (3.2)$$

3.3 Surface thermodynamics

The chemical potential is expressed through thermodynamic equations of the Gibbs energy, but it has to be referred to the quantum chemical energy of the species it is applied for:

$$\mu_i(p_i, T) = E_{i,\mathrm{electr.}} + \Delta\mu_i^{p^0}(T) + kT\ln\frac{p_i}{p^0}. \quad (3.3)$$

The first term in Eq. 3.3 refers to the electronic energy of species i, which is equivalent to the Gibbs energy at 0 K, neglecting the energy change due to vibrations and rotations. The third term is the pressure dependence of the chemical potential. The second term contains all temperature dependent free energy contributions, and it is calculated, based on standard enthalpy and entropy values at $p^0 = 1atm$, as:

$$\Delta\mu_{0\to T} = (H^\circ_{298.15} - H^\circ_0) + (H^\circ - H^\circ_{298.15}) - S^\circ T. \quad (3.4)$$

The terms of Eq. 3.4 are obtained from tabulated values for thermodynamics listed in the NIST database [198]. The first term is necessary since the data are referred to the standard temperature. It is evaluated by summation over the vibrational levels of the ground electronic state of the gas and is given as a constant value specific for the considered gas [199]. The second and third terms are expressed in the form of polynomials, after fitting to experimental values:

$$H^\circ - H^\circ_{298.15} = At + \frac{Bt^2}{2} + \frac{Ct^3}{3} + \frac{Dt^4}{4} - \frac{E}{t} + F - H, \quad (3.5)$$

$$S^\circ = A\ln t + Bt + \frac{Ct^2}{2} + \frac{Dt^3}{3} - \frac{E}{2t^2} + G. \quad (3.6)$$

In equations 3.5 and 3.6, t is an expression of temperature in Kelvin, $t = \frac{T[\mathrm{K}]}{1000}$, and the factors A to H are values yielding $H^\circ - H^\circ_{298.15}$ in kJ/mol and S° in J/molK. The values, for the HF gas, used to calculate $\Delta\mu_i^{p^0}(T)$ in this work are given in table 3.3.
Using Eq. 3.3 for the expression of the chemical potential and following the considerations described in section 2.5, the surface energy γ for the system MF_2/HF at finite temperature

and pressure is calculated via:

$$\gamma(T, p_{\mathrm{HF}}) = \frac{1}{2A}\Big(E_{\mathrm{slab}}^{\mathrm{DFT}} - N_{\mathrm{M}} E_{\mathrm{bulk}}^{\mathrm{DFT}} - N_{\mathrm{HF}}\mu_{\mathrm{HF}}\Big). \tag{3.7}$$

Table 3.3: A - H values for HF gas used to calculate $\Delta\mu_i^{p^0}(T)$. The quantity $H^\circ_{298.15} - H^\circ_0$ is in kJ/mol.

A ($\mathrm{Jmol^{-1}K^{-1}}$)	30.11693
B ($\mathrm{Jmol^{-1}K^{-2}}$)	-3.246613
C ($\mathrm{Jmol^{-1}K^{-3}}$)	2.868116
D ($\mathrm{Jmol^{-1}K^{-4}}$)	-1.243874
E ($\mathrm{kJKmol^{-1}}$)	-0.024861
F ($\mathrm{kJmol^{-1}}$)	-281.4912
G ($\mathrm{Jmol^{-1}K^{-1}}$)	210.9226
H ($\mathrm{kJmol^{-1}}$)	-272.5462
$H^\circ_{298.15} - H^\circ_0$	8.599

4 Publications

The following chapter includes the scientific papers published in the framework of this dissertation. Two of these publications are concerned with investigations on zinc fluoride nanomaterials and are denoted by P1 and P2. The other two publications, P3 and P4, discuss the outcomes of the investigations on group II metal fluorides. For each publication, the contributions by the individual authors are provided.

Paper P1

"A computational Study of the Structure of Zinc Fluoride Surfaces"

Z. Kaawar and B. Paulus

AIP Conf. Proc., **1653**, 020051 (2015)

DOI 10.1063/1.4914242
URL `http://dx.doi.org/10.1063/1.4914242`

Author contributions I did the first principle calculations to investigate the stability and the shape of ZnF_2 crystals in vacuum. Beate Paulus and I discussed the final results. The manuscript was written by myself.

Paper P2

"Theoretical investigations of the CO adsorption on ZnF_2 surfaces"

Z. Kaawar, C. Müller and B. Paulus

Surface Science **656**, 48-53 (2017)

DOI 10.1016/j.susc.2016.06.021
URL `http://dx.doi.org/10.1016/j.susc.2016.06.021`

Author contributions I performed the periodic calculations (CRYSTAL and CRYSCOR calculations) to investigate the Lewis acidity of unsaturated surface cations of ZnF_2. The results were discussed by all the authors. The first version of the manuscript was written by myself, and Carsten Müller contributed to the final version of the manuscript.

Paper P3

"On the morphology of Group II Metal Fluoride Nanocrystals at Finite Temperature and Partial Pressure of HF"

Z. Kaawar, S. Mahn, E. Kemnitz and B. Paulus

Molecules **22**, 663 (2017)

DOI 10.3390/molecules22040663
URL `https://doi.org/10.3390/molecules22040663`

Author contributions All calculations were performed by myself. Stefan Mahn carried out the experimental investigations, comprising the synthesis and characterization of the nanoparticles. Erhard Kemnitz and Beate Paulus conducted the project for its entire duration. The discussion of the results was a join effort of all the coauthors. Stefan Mahn and I wrote the manuscript, with the main contributions done by myself. All authors added contributions to the final version of the publication.

Paper P4

"Adsorption of hydrogen fluoride on alkaline earth fluorides surfaces: a first-principles study"

Z. Kaawar and B. Paulus

will be submitted soon to *"Journal of Fluorine Chemistry"*

Author contributions I performed the periodic calculations to investigate the adsorption of hydrogen fluoride on alkaline earth fluorides surfaces. The discussion of the results was done by both authors. I wrote the manuscript. Beate Paulus added contributions to the final version of the publication.

Adsorption of hydrogen fluoride on alkaline earth fluoride surfaces: a first-principles study

Zeinab Kaawar*, Beate Paulus*

[a] *Institut für Chemie und Biochemie, Freie Universität Berlin, Takustr. 3, D-14195 Berlin, Germany*

Abstract

We have performed periodic calculations for the adsorption of hydrogen fluoride on the three low index surfaces (111), (110) and (100) of alkaline earth metal fluorides MF_2 (M = Ca, Sr and Ba). Adsorption energies were calculated using the two density functionals PBE and PBE0, Hartree-Fock and dispersion correction to PBE. We found that PBE and PBE0 yield similar adsorption energies, both predicting stronger adsorption than Hartree-Fock, and the largest energies were calculated with PBE-D3 correction. Adsorption structures and energies are discussed for different HF coverages, at the PBE level. The interactions of HF with the surface fluorine anions, as well as the interactions among the adsorbed HF molecules are found to play a crucial role in the adsorption process.

Keywords: periodic calculations, HF adsorption, MF_2 surfaces, hydrogen bonds.

1. Introduction

Fluorite-type materials hold a special place in technologically promising compounds. Among these, alkaline earth fluorides MF_2 (M = Ca, Sr and Ba) are of significant interest due to their exceptional properties which allow their applicability in many fields ranging from optics [1–3], spectroscopy [4, 5], dentistry [6, 7]

*Corresponding author
Email address: kaawarzeinab@zedat.fu-berlin.de (Zeinab Kaawar)

to heterogeneous catalysis [8]. The need for such materials in industry urged scientists to find a versatile path to their synthesis. A variety of synthetic approaches has been introduced for the preparation of MF_2 nanoparticles, such as solvothermal process, the reverse micelle method, different precipitation methods, the mechanochemical route and the fluorolytic sol-gel procedure [9–22]. The latter has proved to be effective and successful over a wide range of fluorides [2, 3, 23–28], including CaF_2, SrF_2 and BaF_2.

It has been shown that sol-gel synthesized MF_2-based nanomaterials exhibit high surface area and distinct acidic properties which allows them to perform as heterogeneous catalysts for Lewis acid catalyzed reactions [29–38]. As an example, high surface area BaF_2 was found to catalyze dehydrochlorination reactions of chlorofluorocarbons [8].

A number of theoretical studies exists for calcium, strontium and barium fluorides. The electronic band structure of these solids has been calculated by means of tight binding linear muffin tin orbital method [39, 40], confirming that the investigated materials are wide band gap insulators. Kanchana et al. [39, 40] also calculated the transition pressures at which these fluorides undergo phase transition from the fluorite to the orthorhombic $PbCl_2$-type structure, as well as metallization pressures where they undergo insulator to metal transition upon compression. Concerning the surface structure of group II fluorides, the reactivity of CaF_2 has been investigated by de Leeuw et al. [41], using DFT calculations with the LDA functional, where water and methanoic acid were adsorbed on the (111) surface.

In our previous work [42], we have shown that the predicted shape of a MF_2 crystal in vacuum is an octahedron, with (111) being the unique surface exposed. We have also proved, with methods of ab initio surface thermodynamics, that the shape of the crystals is strongly affected by the temperature and the pressure of hydrogen fluoride, where other surfaces are also exposed. The aim of this work is to investigate the interaction of hydrogen fluoride molecules with the low-index surfaces of CaF_2, SrF_2 and BaF_2, which is of relevance in the production of the nanomaterials as hydrogen fluoride is a reactant in the synthetic

procedure. For this purpose, we have studied the adsorption of HF on MF_2 low index surfaces at various coverages, using different methods. We describe first, in Section 2, the computational parameters and the approaches used in our calculations. The performance of the different methods used in the calculation of adsorption energies at full coverage is discussed in Section 3. In Section 4.1, we discuss the adsorption structures optimized at the PBE level. We present the entire set of adsorption energies calculated at full, half and 25 % coverages using PBE in Section 4.2, where the effect of the HF-HF interaction on the adsorption structures and energies is also discussed.

2. Computational details

2.1. Calculation of the adsorption energy

The adsorption energies reported in the following sections have been calculated according to:

$$E_{\mathrm{ads}} = \frac{1}{N}\left[E\left(\mathrm{s}+\mathrm{ads}\right) - E\left(\mathrm{s}+\mathrm{GF}_{\mathrm{ads}}\right) - E\left(\mathrm{ads}+\mathrm{GF}_{\mathrm{s}}\right) - \Delta E_{\mathrm{rel}}\left(\mathrm{s}\right) - \mathrm{N}\Delta E_{\mathrm{rel}}\left(\mathrm{ads}\right)\right].$$

Correction for the basis set superposition error (BSSE) within the counterpoise scheme and the relaxation effects has been applied. The first term in the equation represents the energy of the periodic system comprising the slab and the adsorbates and it is calculated at the relaxed structure. The second and third terms $E(\mathrm{s}+\mathrm{GF}_{\mathrm{ads}})$ and $E(\mathrm{ads}+\mathrm{GF}_{\mathrm{s}})$ refer to the BSSE corrected energies of the slab and the adsorbant obtained by replacing the adsorbates and the slab, respectively, by ghost functions. The BSSE corrected energies are computed in two single point calculations at the optimized structure of the joint system. ΔE_{rel} is the relaxation energy during adsorption and is calculated by substracting the energy of the component (slab or adsorbate) in the adsorption structure from the energy of its relaxed free structure. The relaxation energy of the adsorbate is computed for one free molecule and multiplied by the number N of adsorbates in the periodic surface unit cell.

2.2. Computaional parameters

Periodic density functional theory calculations were carried out using the CRYSTAL09 code [43, 44]. In a previous work [42], we have shown that the PBE functional [45] performs reasonably well for the ground state bulk properties of CaF_2, SrF_2 and BaF_2, overestimating the experimental lattice constant at most by 0.7 %. This functional has also yielded surface energies for the natural cleavage plane (111) of the considered materials which were in very good agreement with the experimental values. Therefore, in the present work, we optimize the adsorption structures of HF on MF_2 surfaces at the PBE level. For testing the performance of other methods for the adsorption energies, we performed additional structure optimizations using the hybrid functional PBE0 and Hartree-Fock, considering only the full coverage case. We also applied Grimme's scheme for dispersion correction on the PBE optimized structures, in a single point calculation, using the DFT-D3 version [46], with the damping function of Becke and Johnson [47].

Relying on earlier surface calculations [42], we employed stoechiometric symmetric slabs with a thickness of two, six and seven MF_2 units for the (111), (110) and (100) surfaces, respectively. We have tested different terminations of the slabs, and only the ones in which a balanced charge distribution is achieved, are stable. This was simulated for the (100) surface by removing one F^- anion from the top and one from the bottom of the slab resulting in the most stable termination for this surface. Adsorption was modelled by placing hydrogen fluoride atop one surface cation, as start configuration (perpendicular to the surface with the fluorine pointing down to the cation at a distance of 2.5Å. For the optimizations of the slabs, the lattice constant optimized previously with PBE is kept fixed and the nuclear coordinates of the symmetric slabs and the adsorbates are relaxed.

The fluorine is described with a valence triple-zeta basis set augmented by a d polarization function (exponent 0.7) [48], previously optimized for the MgF_2 solid. The metal atoms are described by scalar relativistic energy-optimized effective core potentials [49] leaving 10 valence electrons to be treated explic-

itly, and a corresponding cc-pVDZ basis set optimized recently in our group for fluorides was employed [50]. For the hydrogen atom, we used a VTZ basis set from a an earlier study on HF adsorption on AlF_3 surfaces [51]. The eigenvector calculation is done using a Pack-Monkhorst grid of 8 k-points along each lattice direction of the irreducible Brillouin zone. The density matrix is calculated for a Gilat net of 16 k-points. The accuracy of bielectronic integrals is controlled by cutoff parameters of 6, 6, 6, 12, 30 and an energy convergence criterion of 10^{-8} Hartree is used in the self-consistent field iterations.

3. Performance of different methods

In this section, we report the adsorption energy of HF on the three low index surfaces (111), (110) and (100) of calcium, strontium and barium fluorides at full coverage, using different methods. We calculated adsorption energies at the PBE, PBE0 and Hartree-Fock levels, with the structures optimized at each level. The energies obtained using PBE were combined with D3 corrections, in single point calculations. Adsorption structures optimized at the PBE0 and Hartree-Fock levels are very similar to the ones optimized at the PBE level which are thoroughly discussed in the next section. The results for the adsorption energies of the three investigated crystals are shown in Table 1. We report negative values of the energies, indicating a stabilizing interaction. In the following, we compare the absolute values of the energies, so that an energy value of *e.g.* -0.40eV is regarded as lower than the one of -0.51eV.

The performance of the different methods used is similar for all three materials. The exchange-correlation functional PBE and the hybrid functional PBE0 yield comparable adsorption energies in the case of CaF_2 and SrF_2, where the discrepancy between both functionals is less than 3%. In the case of BaF_2, PBE0 predicts somewhat weaker adsorption than PBE. Calculations using Hartree-Fock result in 18-32% weaker adsorption compared to PBE. (This difference is found to be 62% for the weak adsorption on the (110) surface of BaF_2). Dispersion correction on PBE adds a contribution of 10-30% to the uncorrected result.

Table 1: Adsorption energies (in eV) of HF per molecule on CaF_2, SrF_2 and BaF_2 surfaces at full coverage, calculated using different methods.

MF_2	Surface	PBE	PBE+D3	PBE0	Hartree-Fock
	(111)	-0.40	-0.51	-0.41	-0.27
CaF_2	(110)	-0.69	-0.79	-0.68	-0.54
	(100)	-0.75	-0.89	-0.77	-0.60
	(111)	-0.49	-0.59	-0.49	-0.35
SrF_2	(110)	-0.76	-0.85	-0.74	-0.61
	(100)	-0.91	-1.03	-0.90	-0.75
	(111)	-0.58	-0.67	-0.52	-0.41
BaF_2	(110)	-0.26	-0.34	-0.18	-0.10
	(100)	-1.04	-1.15	-0.94	-0.82

The influence of both, dispersion and exact exchange, is weak for the adsorption of HF on MF_2 surfaces. Even the correlation contributions are between 20 and 40% only comparing Hartree-Fock and PBE-D3 values. So, we can conclude that the main interaction is due to electrostatics, well captured with all methods applied.

4. Adsorption of HF at different coverages

We have shown in the previous section that PBE and PBE0 perform similarly for the description of the HF adsorption. Therefore, we use the less costly exchange-correlation functional PBE to complete the set of our calculations. So, we discuss in this section the adsorption of HF for three different coverages: full, half and 25%. This allows a better understanding of the influence of the HF-HF interaction on the adsorption structures and energies.

4.1. Adsorption structures

PBE-optimized adsorption structures of HF on CaF_2, SrF_2 and BaF_2 surfaces are shown in figures 1, 2 and 3, respectively. In all cases, the adsorbates are oriented in such a way that the fluorine atom is placed above the coordinatively unsaturated metal ion, and the hydrogen of the adsorbate points towards the surface forming a hydrogen bond with a surface fluorine atom. The distance between the adsorbate's fluorine and the surface metal is in the range of 2.3-2.8Å depending on the surface and HF coverage (see Table 2). The distance of the adsorbate's hydrogen to its nearest surface fluorine varies between 1.2 and 1.6Å indicating the formation of strong hydrogen bonds, except for the full coverage adsorption on the (110) surface of BaF_2, where the hydrogen forms two weaker hydrogen bonds with two equivalent surface fluorines with a distance of 2.3Å. The interatomic distance of HF increases due to adsorption, with respect to the free HF, with the largest elongations calculated for the (100) surface of all three crystals. Here, the HF molecule is elongated by 0.22Å and the hydrogen lies at equal distance, which is found to be 1.16Å, between the surface fluorine and the adsorbate's fluorine. For the full HF coverage on the (100) surface of CaF_2, the HF bond is elongated by 0.13Å and the distance between the hydrogen and the surface fluorine is 1.27Å. For adsorption on surfaces (111) and (110), the elongations of the HF bond vary between 0.01-0.13Å, depending on the coverage. The presence of the adsorbates affects the structure of the surfaces, where the surface ions are displaced from their original positions with respect to the optimized clean surface. The displacements of the surface metal cations and the fluorine anions in a direction perpendicular to the surface plane are in the ranges of 0.007-0.09Å and 0.004-0.09Å, respectively. This effect is mostly pronounced in the case of 25% coverage where a slight distortion of the uppermost surface layer consisting of fluorine is observed. That is due to the displacements of some surface fluorines outwards (towards the vacuum) and of others inwards (towards the bulk). For example, in the case of 25% coverage on the (111) surface, the surface fluorines forming a hydrogen bond with the adsorbate's hydrogen are displaced outwards by 0.33Å and the other fluorines

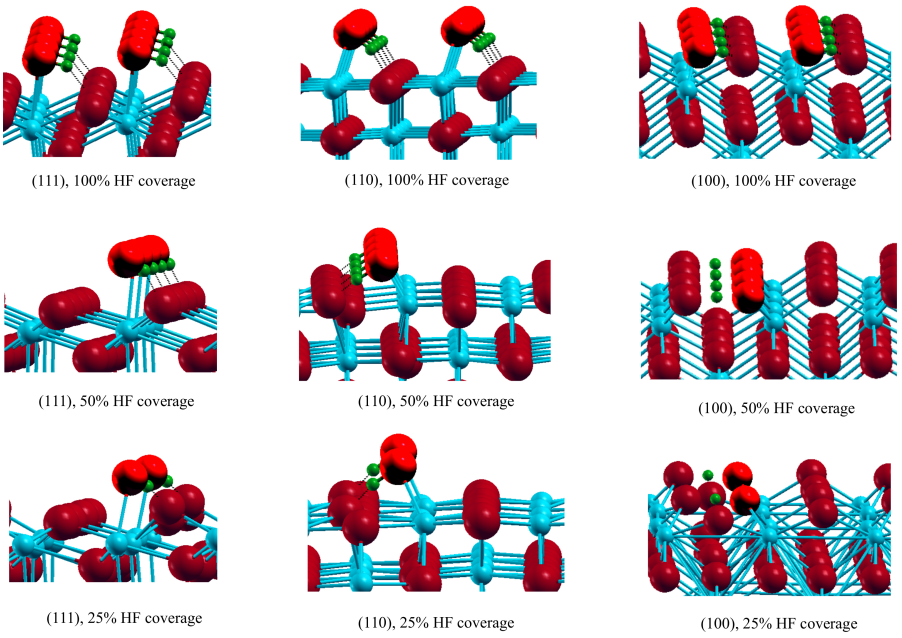

Figure 1: Adsorption structures of HF on CaF_2 surfaces at 100%, 50% and 25% coverages, obtained using PBE. Calcium atoms are represented as blue, fluorine as red and hydrogen as green spheres. The fluorines of the adsorbates are highlighted.

in the row are shifted inwards by 0.09Å, leading to a zig-zag form of the outer layer. The Mulliken population analysis indicates that a charge transfer from the surface to the adsorbate is occuring. The electron density increase on the adsorbate varies between 0.07 and 0.3 *a.u.*, and it increases with decreasing coverage.

4.2. Adsorption energies

Adsorption energies calculated with PBE for CaF_2, SrF_2 and BaF_2 surfaces are listed in Table 2. We observe a decrease in the adsorption energy with increasing coverage (weaker binding), likely due to the repulsive interaction between the adsorbates at higher coverage. The energy difference between coverages strongly depends on the surface structure, i.e. the arrangement of

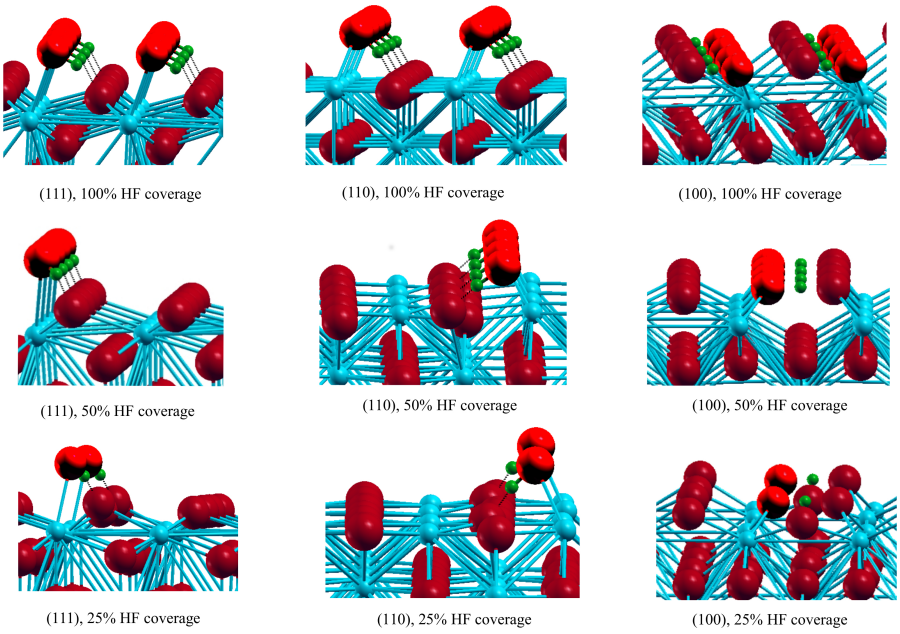

Figure 2: Adsorption structures of HF on SrF_2 surfaces at 100%, 50% and 25% coverages, obtained using PBE. Strontium atoms are represented as blue, fluorine as red and hydrogen as green spheres. The fluorines of the adsorbates are highlighted.

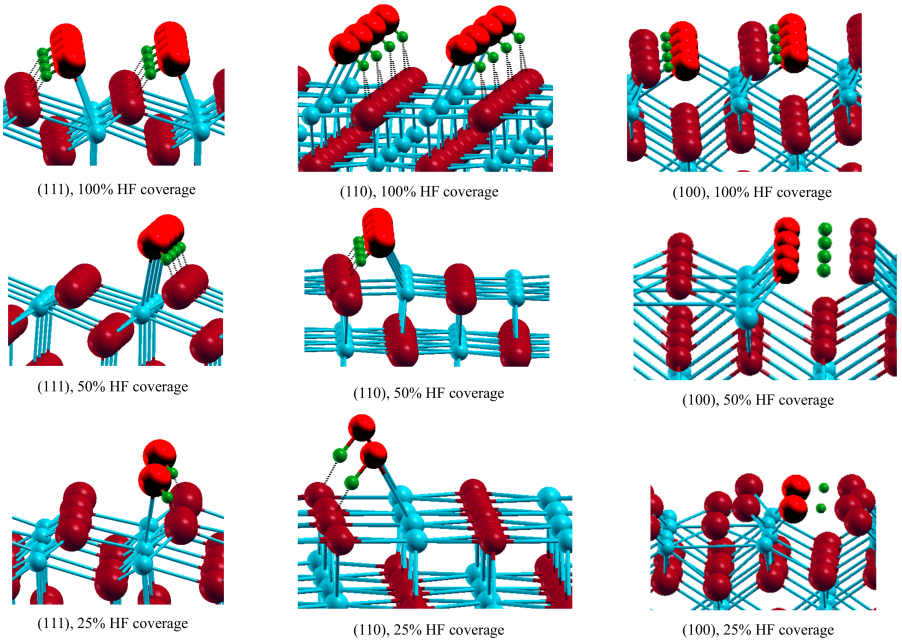

Figure 3: Adsorption structures of HF on BaF_2 surfaces at 100%, 50% and 25% coverages, obtained using PBE. Barium atoms are represented as blue, fluorine as red and hydrogen as green spheres. The fluorines of the adsorbates are highlighted.

the adsorption sites on the surface. For surface (111), the energy difference between full and half coverages is about 0.1eV and a further decrease of the coverage to 25% results in stronger adsorption by 0.1-0.14eV compared to half coverage. Indeed, this surface has a square unit cell and thus, the adsorbates are uniformely placed on the adsorption sites. However, at full coverage, the HF molecules are adsorbed on the coordinatively unsaturated surface cations with the distance separating the fluorine of an adsorbate and the hydrogen of another neighbouring one being 3.14-3.76Å, which favors the interaction between the adsorbing molecules and destabilizes the adsorption of a full monolayer of HF on this surface. Half coverage is reached by removing the HF molecules in the direction where they are closest to each other. At 25% coverage, every second HF molecule in the other direction is removed, leading to a stabilization of the adsorption structure and therefore a larger adsorption energy. Adsorption energies on surface (110) are more affected by coverage than (111), presumably due to the rectangular unit cell of this surface, which favors a denser arrangement of adsorption sites in one periodic direction than the other. The energy difference between coverages on this surface is most pronounced in the case of BaF_2, where the adsorption energy increases by 0.73eV upon lowering coverage from full to half. The HF molecules adsorbed in full coverage form two hydrogen bonds with the surface, which implies a stronger interaction between the hydrogens and the surface fluorines and thus a weaker adsorption on the surface cations. At half coverage, this interaction is reduced and a stronger adsorption occurs. For 25% coverage, the adsorption energy is slightly higher than that at 50%. The most significant effect of the coverage on the adsorption energies is found for the (100) surface. The arrangement and orientation of the adsorbates on the adsorption sites are found to play a significant role in the behaviour of the adsorption energies. As already discussed in section 4.1, adsorption on this surface results in large elongations of the intramolecular bond of HF, which makes the hydrogen very close to the surface fluorine. At half coverage, a row of HF molecules is removed leading to the minimization of the interaction between the hydrogen and the fluorines of the surfaces compared to full coverage.

Table 2: Adsorption energies (in eV) of HF per molecule on CaF_2, SrF_2 and BaF_2 surfaces at 100 %, 50 % and 25 % coverages, calculated using PBE. The distance between the metal ion and the fluorine of the adsorbate, the intramolecular distance of HF and the distance between the hydrogen and the surface fluorine are also given (in Å).

MF_2	Surface	Coverage (%)	E_{ads} [eV]	d_{M-F} [Å]	d_{H-F} [Å]	$d_{H-F_{slab}}$ [Å]
CaF_2	(111)	100	-0.40	2.48	0.98	1.56
		50	-0.48	2.46	1.00	1.47
		25	-0.62	2.34	1.03	1.33
	(110)	100	-0.69	2.40	1.01	1.43
		50	-0.90	2.30	1.07	1.27
		25	-0.99	2.36	1.05	1.33
	(100)	100	-0.75	2.31	1.07	1.27
		50	-1.28	2.45	1.16	1.16
		25	-1.34	2.40	1.16	1.16
SrF_2	(111)	100	-0.49	2.61	0.99	1.54
		50	-0.58	2.63	1.00	1.44
		25	-0.67	2.56	1.02	1.37
	(110)	100	-0.76	2.60	1.01	1.42
		50	-0.88	2.49	1.07	1.27
		25	-0.93	2.56	1.05	1.32
	(100)	100	-0.91	2.44	1.15	1.16
		50	-1.46	2.63	1.16	1.16
		25	-1.42	2.55	1.16	1.16
BaF_2	(111)	100	-0.58	2.78	0.99	1.50
		50	-0.69	2.81	1.01	1.41
		25	-0.80	2.81	1.02	1.37
	(110)	100	-0.26	2.84	0.95	2.31
		50	-0.99	2.76	1.05	1.32
		25	-1.12	2.80	1.04	1.33
	(100)	100	-1.04	2.82	1.15	1.16
		50	-1.59	2.80	1.16	1.16
		25	-1.69	2.77	1.16	1.16

Indeed, the hydrogen is closer to the surface fluorine than in the full coverage case which favors in principle the interaction between them. However, the HF molecule is dissociated and the fluorine of the adsorbate is strongly bound to the surface, leading to higher adsorption energies, by about 0.5eV, at half coverage. The 25 % coverage case resembles the 50% one, showing only slightly higher adsorption energies. In the case of adsorption on SrF_2, the adsorption energy at 25% coverage is slightly lower than that at 50% coverage.

Comparing the general trends of the adsorption energies on the three different surfaces, the strongest adsorption is found to occur on the six-fold coordinated metal cations of the least stable (100) surface, followed by the six-fold coordinated cations of (110). The weakest adsorption takes place at the seven-fold coordinated cations of (111), which is the most stable surface. A comparison between the three investigated materials reveals, with exception of the full coverage case on the (110) surface, that adsorption on BaF_2 surfaces is the strongest, followed by SrF_2 and CaF_2 surfaces. This can be related to the electronegativity of the metals. Calcium is more electronegative than strontium and barium, so the Ca-F bond is less polar, which leads to a higher electron density on Ca^{2+} (compared to Sr^{2+} and Ba^{2+}). As a result, adsorption on Ca^{2+} sites is weaker. In general, the values of the adsorption energies vary between -0.4 and -1.7eV, indicating a chemisorption on the surfaces in most of the cases.

5. Conclusion

We have investigated in this work the adsorption of hydrogen fluoride on CaF_2, SrF_2 and BaF_2 surfaces. We have used density functional theory with PBE and PBE0, Hartree-Fock and dispersion correction (D3) on PBE to calculate adsorption energies at full HF coverage. All methods applied catch the same trends in the adsorption energies for all three investigated materials. In most of the cases, comparable adsorption energies are obtained with the exchange-correlation functional PBE and the hybrid functional PBE0, and a slightly stronger adsorption is predicted with PBE-D3. This illustrates the weak ef-

fect of dispersion and exact exchange on the adsorption of HF, which is mainly governed by electrostatics. Using PBE, we have discussed the adsorption structures and energies at different coverages and found that adsorption becomes stronger upon lowering coverage. That is presumably due to the effect of the interactions among the adsorbates, and the strength of the interaction between the hydrogen and the surface fluorines as well. In general, the calculated adsorption energies and structures indicate that the interaction of HF with surfaces is brought by a chemisorption process.

6. Acknowledgment

We thank the Deutsche Forschungsgemeinschaft (DFG) (through the research training network "Fluorine as a key element", GRK 1582) for financial support of this study, and the HLRN (Norddeutscher Verbund für Hoch- und Hoöchstleistungsrechnen) as well as the ZEDAT (Zentraleinrichtung für Datenverarbeitung) at the Freie Universität Berlin for computational resources and support. We gratefully acknowledge our experimental collaborator Prof. Dr. Erhard Kemnitz (Humboldt University, Berlin) and Dr. Carsten Müller for fruitful discussions.

References

[1] Krüger, H.; Hertwig, A.; Beck, U.; Kemnitz, E. *Thin Solid Films* **2010**, *518*, 6080–6086.

[2] Rehmer, A.; Scheurell, K.; Kemnitz, E. *J. Mater. Chem. C* **2015**, *3*, 1716–1723.

[3] Schmidt, L.; Emmerling, F.; Kirmse, H.; Kemnitz, E. *RSC Adv.* **2014**, *4*, 32–38.

[4] Kawano, K.; Ohya, T.; Tsurumi, T.; Katoh, K.; Nakata, R. *Phys. Rev. B* **1999**, *60*, 11984.

[5] Ikesue, A.; Aung, Y. L. *Nat. Photonics* **2008**, *2*, 721–727.

[6] Ling, L.; Xu, X.; Choi, G. Y.; Billodeaux, D.; Guo, G.; Diwan, R. M. *J. Dent. Res.* **2009**, *88(1)*, 83–88.

[7] Xu, H. H. K.; Moreau, J. L.; Sun, L.; Chow, L. C. *J. Dent. Res.* **2010**, *89(7)*, 739–745.

[8] Teinz, K.; Wuttke, S.; Börno, F.; Eicher, J.; Kemnitz, E. *Journal of Catalysis* **2011**, *282*, 175–182.

[9] Fujihara, S.; Kadota, Y.; Kimura, T. *J. Sol-gel Sci. Technol.* **2002**, *24*, 147–154.

[10] Hong, B. C.; Kawano, C. *J. Alloys. Compd.* **2006**, *838*, 408–412.

[11] Hong, B. C.; Kawano, C. *Opt. Mater.* **2008**, *30*, 952.

[12] Patil, P. T.; Dimitrov, A.; Radnikb, J.; Kemnitz, E. *J. Mater. Chem.* **2008**, *18*, 1632.

[13] Kumar, G. A.; Chen, C. W.; Ballato, J.; Riman, R. E. *Chem. Mater.* **2007**, *19*, 1523.

[14] Zhang, X.; Quan, Z.; Yang, J.; Yang, P.; Lian, H.; Lin, J. *Nanotechnology* **2008**, *19*, 075603.

[15] Bensalah, A.; Mortier, M.; Patriarche, G.; Gredin, P.; Vivien, D. *Journal of Solid State Chemistry* **2006**, *179*, 2636–2644.

[16] Sun, X.; Li, Y. *Chem. Commun.* **2003**, *14*, 1768–1769.

[17] Wang, F.; Fan, X.; Pi, D.; Wang, M. *Solid State Communications* **2005**, *133*, 775–779.

[18] Chauhan, S. M.; Chakrabarti, B. S. *Int. J. Eng. Res. & Technol.* **2014**, *3*, 129–131.

[19] Wang, L.; Wang, B.; Wang, X.; Lu, W. *Opt. Mater.* **2007**, *29*, 1179–1185.

[20] Tahvildari, K.; pour, M. E.; Ghammamy, S.; Nabipour, H. *International Journal of Nano Dimension* **2012**, *2*, 269–273.

[21] M. Dreger, G. S.; Kemnitz, E. *Solid State Sciences* **2011**, *14*, 528–534.

[22] Groß, U.; Rüdiger, S.; Kemnitz, E. *Solid State Sciences* **2007**, *9*, 838–842.

[23] Kemnitz, E.; Groß, U.; Rüdiger, S.; Shakar, S. C. *Angew. Chem., Int. Ed.* **2003**, *42*, 4251–4254.

[24] Rüdiger, S.; Groß, U.; Feist, M.; Prescott, H. A.; Shakar, S. C.; Troyanov, S. I.; Kemnitz, E. *J. Mater. Chem.* **2005**, *15*, 588–597.

[25] Rüdiger, S.; Groß, U.; Kemnitz, E. *J. Fluorine Chem.* **2007**, *128*, 353–368.

[26] Nickkho-Amiry, M.; Eltanany, G.; Wuttke, S.; Rüdiger, S.; Kemnitz, E.; Winfield, J. M. *J. Fluorine Chem.* **2008**, *129*, 366–375.

[27] Guo, Y.; Wuttke, S.; Vimont, A.; Daturi, M.; Lavalley, J. C.; Teinz, K.; Kemnitz, E. *J. Mater. Chem.* **2012**, *22*, 14587.

[28] Kemnitz, E. *Catal. Sci. Technol.* **2015**, *5*, 786–806.

[29] Candu, N.; Wuttke, S.; Kemnitz, E.; Coman, S. M.; Parvulescu, V. I. *Appl. Catal. A* **2011**, *391*, 169–174.

[30] Coman, S. M.; Wuttke, S.; Vimont, A.; Daturi, M.; Kemnitz, E. *Adv. Synth. Catal.* **2008**, *350*, 2517–2524.

[31] Coman, S. M.; Parvulescu, V. I.; Wuttke, S.; Kemnitz, E. *ChemCatChem* **2010**, *2*, 92–97.

[32] Negoi, A.; Wuttke, S.; Kemnitz, E.; Macovei, D.; Parvulescu, V. I.; Teodorescu, C. M.; Coman, S. M. *Angew. Chem. Int. Ed.* **2010**, *49*, 8134–8138.

[33] Coman, S. M.; Patil, P.; Wuttke, S.; Kemnitz, E. *Chem. Commun.* **2009**, 460–462.

[34] Troncea, S. B.; Wuttke, S.; Kemnitz, E.; Coman, S. M.; Parvulescu, V. I. *Appl. Catal. B* **2011**, *107*, 260–267.

[35] Kemnitz, E.; Wuttke, S.; Coman, S. M. *Eur. J. Inorg. Chem* **2011**, 4773–4794.

[36] Rüdiger, S.; Kemnitz, E. *Dalton Trans.* **2008**, 117–1127.

[37] Prescott, H. A.; Li, Z.-J.; Kemnitz, E.; Deutsch, J.; Lieske, H. *J. Mater. Chem* **2005**, *15*, 4616–4628.

[38] Wuttke, S.; Coman, S. M.; Kröhnert, J.; Jentoft, F. C.; Kemnitz, E. *Catal. Today* **2010**, *152*, 2–10.

[39] Kanchana, V.; Vaitheeswaran, G.; Rajagopalan, M. *Physica B* **2003**, *328*, 283.

[40] Kanchana, V.; Vaitheeswaran, G.; Rajagopalan, M. *Journal of Alloys and Compounds* **2003**, *359*, 66.

[41] de Leeuw, N. H.; Cooper, T. G. *J. Mater. Chem.* **2003**, *13*, 93.

[42] Kaawar, Z.; Mahn, S.; Kemnitz, E.; Paulus, B. *Molecules* **2017**, *22*.

[43] Dovesi, R.; Orlando, R.; Civalleri, B.; Roetti, C.; Saunders, V. R.; Zicovich-Wilson, C. M. *Z. Kristallogr.* **2005**, *220*, 571–573.

[44] Dovesi, R.; Saunders, V.; Roetti, C.; Orlando, R.; Zicovich-Wilson, C. M.; Pascale, F.; Civalleri, B.; Doll, K.; Harrison, N.; Bush, I.; D'Arco, P.; Llunell, M. CRYSTAL09 User's Manual, University of Torino, Torino. 2010.

[45] Perdew, J. P.; Burke, K.; Ernzerhof, M. *Phys. Rev. Lett.* **1996**, *77*, 3865–3868.

[46] Grimme, S.; Antony, J.; Ehrlich, S.; Krieg, H. *J. Chem. Phys.* **2010**, *132*, 154104.

[47] Becke, A. D.; Johnson, E. R. *J. Chem. Phys.* **2005**, *123*, 154101.

[48] Huesges, Z.; Müller, C.; Paulus, B.; Maschio, L. *Surf. Sci.* **2014**, *627*, 11–15.

[49] Kaupp, M.; v R. Schleyer, P.; Stoll, H.; Preuss, H. *J. Chem. Phys.* **1991**, *94*, 1360.

[50] Belger, D.; Huesges, Z.; Voloshina, E.; Paulus, B. *J. Phys.: Condens. Matter* **2010**, *22*, 275504.

[51] Bailey, C.; Mukhopadhyay, S.; Wander, A.; Searle, B.; Harrison, N. *J. Phys. Chem. C* **2009**, *113*, 4976.

5 Summary

An increasing demand on size-controllable, highly active, large surface area nanomaterials has emerged in the last decades. A search for such materials has become essential in human activity and industrialization, due to their widespread application in chemistry, physics and biology. Nanostructured metal fluorides represent an important class of these technologically promising materials, due to their optical and catalytic properties. The latter are mainly related to the surface properties of the material, and thus, knowing the surface structure, stability and reactivity is crucial for understanding the functionality of the material. The aim of this thesis was to gain deeper insights into the factors controlling the surface properties of metal fluorides. For this purpose, a theoretical model for a set of divalent metal fluorides was developed towards answering two principal questions: Which factors contribute to the catalytic activity of nanoscopic metal fluorides, and how is the morphology of the crystals affected by temperature and pressure. First, I investigated the structure and properties of the considered materials with the use of quantum chemical methods. This was done by calculating key properties, like bulk parameters, surface energies and adsorption energies. Second, I predicted the morphology of the crystals under different synthetic conditions, through modeling the influence of temperature and HF pressure on the stability of metal fluoride surfaces. The end-point of these theoretical investigations was the validation of the developed models by the experimental findings. The purpose of this chapter is to summarize the main outcomes of these investigations that are published in four papers P1-P4.
Motivated by the interesting catalytic properties of the sol-gel synthesized MgF_2 nanomaterial, I started my investigation with the structurally similar ZnF_2 which has been also synthesized in a fluorolytic sol-gel procedure [25]. In Paper P1, we performed periodic bulk optimizations as a starting point of the calculations, and periodic slab optimizations to evaluate the surface energies and relative surface stabilities of ZnF_2 low-index surfaces, using density functional theory. Based on the calculated surface energies, the shape of a ZnF_2 crystal has been predicted following the so-called Wulff procedure. In this first publication, two different structures, the rutile and the $CaCl_2$-type, were considered. We found that the two structures have similar bulk parameters and surface stabilities, although they belong to two different lattice systems, tetragonal and orthorhombic. The (110) was found to be the most stable surface with the lowest surface energy. The surface area of a ZnF_2 nanocrystal in vacuum was found to expose the (101), (110) and (100) surfaces, without any contributions of the (111) and (001) surfaces.

To understand the catalytic performance of the material, it is crucial to study the Lewis acidity of its surface cations. Indeed, coordinatively unsaturated cations on the surfaces have a lower number of binding neighbours compared to the coordination sphere in the bulk solid

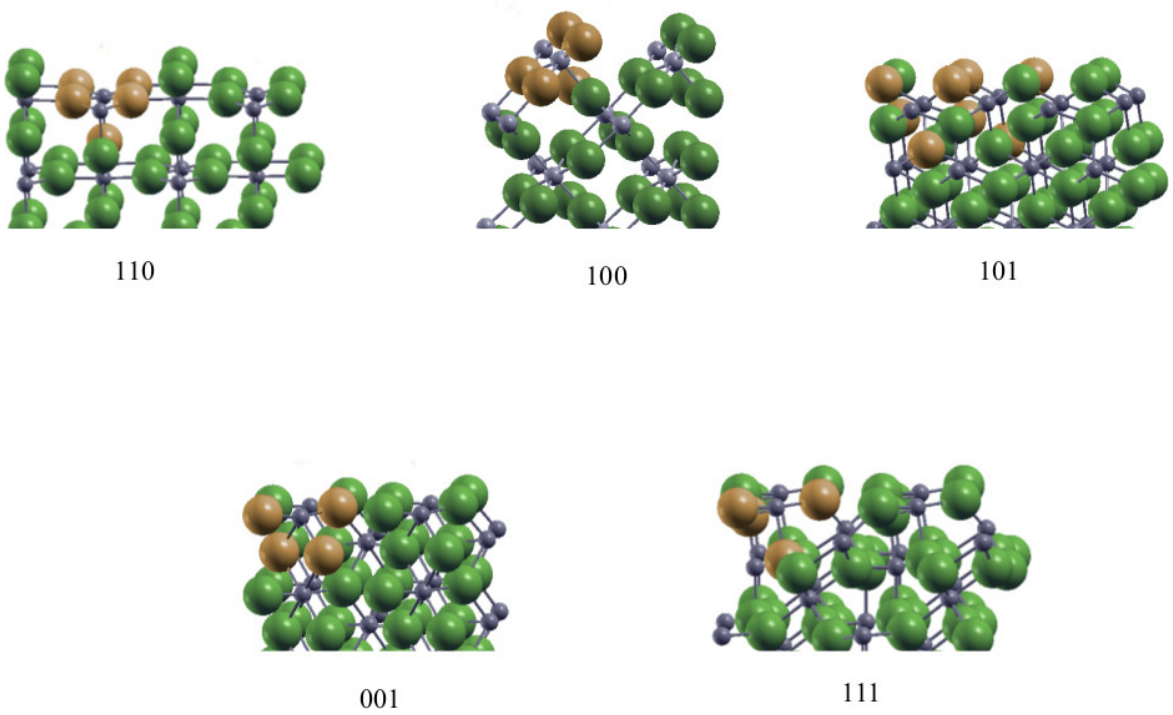

Figure 5.1: Low index ZnF_2 surfaces. Zinc atoms are represented in grey and fluorine in green. The coordination sphere around the surface cations is shown in brown.

and are thus electron-poor (Lewis acidic) sites. This results in a high catalytic activity of the acidic material. The coordination sphere around the surface cations of the five low index ZnF_2 surfaces is shown in Fig. 5.1. The (110) and the (100) surfaces, which are the most two stable surfaces, expose fivefold coordinated zinc ions, whereas the less stable (001) and (111) surfaces expose fourfold coordinated cations. In the (101) surface, two types of unsaturated surface cations, one fourfold and one fivefold coordinated, are found. For evaluating the Lewis acidity of the surface cations, these low index surfaces were characterized with CO adsorption using periodic calculations at different levels of theory, the results of which were discussed and published in Paper P2. Adsorption energies of CO were calculated using B3LYP, dispersion correction to B3LYP (D2 and D3), Hartree-Fock and LMP2, for the sake of comparing the performance of different methods. B3LYP was found to adequatly describe the CO adsorption, performing well compared to LMP2, while dispersion corrections strongly overestimate the adsorption energy. A general trend was observed for all the surfaces: the adsorption energy increases with decreasing coverage. That is strongly influenced by the interactions among the adsorbed CO molecules, which have shown to play an important role in the adsorption process. In addition to the adsorption energies, we calculated vibrational frequency shifts of the adsorbed CO molecules with respect to the free CO molecule, using B3LYP. The results of the adsorption energies and frequency shifts, at full and half coverages, are presented in table 5.1. As a powerful tool for the characterization of surface cations, the adsorption of probe molecules such as CO leads to small changes in the electronic structure of the adsorbed molecules, which can be manifested in shifts of the vibrational frequencies measured in Infrared spectroscopy (IR). Guo et al. [25] studied the Lewis acidity of sol-gel

Table 5.1: Adsorption energies (eV) and vibrational frequency shifts (in cm^{-1}) of CO adsorbed on ZnF_2 surfaces, calculated at the B3LYP level. θ represents the coverage, and CN the coordination number of the surface cations.

Surface	CN	E_{ads} [eV]		Freq. shift [cm^{-1}]	
		$\theta = 1.0$	$\theta = 0.5$	$\theta = 1.0$	$\theta = 0.5$
(110)	5	-0.23	-0.30	64	67
(100)	5	-0.14	-0.19	43	43
(101)	5,4	-0.13	-0.27	31	64
(001)	4	-0.21	-0.27	54	55
(111)	4	-	-0.22	-	32

prepared ZnF_2 by measuring in IR the vibrational frequencies of adsorbed carbon monoxide molecules. They observed three distinct bands for the CO frequency mode and assigned them to different coordinatively unsaturated Zn^{2+} cations. For small doses of CO, the band with highest wave number was observed and the one with lowest wave number showed up at very high pressure of CO. The calculated vibrational frequency shifts validate the experimental findings: at low CO coverage, higher frequency shifts were calculated, indicating a stronger adsorption. However, theoretical calculations predicted that cations on different surfaces but having the same coordination number can have different Lewis acidity. That deviates from the experimental suggestion that relates the Lewis acidity to the number of missing coordination partners of the surface cation and assumes that, the less neighbors the cation has, the higher is its Lewis acidity. It has also been suggested that less stable surfaces expose generally cations of higher Lewis acidity. That was not fully supported by the results of the calculations: the calculated adsorption energies and frequency shifts have shown some deviations in the trend with respect to the order of stability of different surfaces.

Compared to MgF_2, a similar system which was investigated in a previous analogous study [200], ZnF_2 shows comparable trends in the adsorption energy and frequency shifts of adsorbed CO. This similarity was also confirmed experimentally [25], where the same types of unsaturated surface cations were found in both strutures indicating a comparable Lewis acidity. However, ZnF_2 was found to be catalytically inactive for the dismutation reaction of chlorofluoromethanes, in contrast to MgF_2 which has revealed an excellent catalytic performance. It is generally assumed that, the catalytic activity of a metal fluoride is somewhat related to the Lewis acidity of the coordinatively unsaturated surface cations, which can be evaluated from the adsorption energy and the frequency shift of a probe molecule on the surface. Nonetheless, numerous factors are involved in the interactions of the surfaces with the adsorbates, as well. The surface structure and composition and the surface anions can be as important as the Lewis acidity of surface cations.

Towards a second direction, this work was aiming at predicting the morphology of metal flu-

Table 5.2: Optimized lattice constant a (Å), bulk modulus B (GPa), cohesive energy E_{coh} (eV) and lattice energy E_{lat} (eV) for CaF_2, SrF_2 and BaF_2 calculated with different methods. Experimental values are given for comparison.

		B3LYP	B3PW	LDA	PBE	PWGGA	Hartree-Fock	Exp.
CaF_2	a [Å]	5.50	5.47	5.33	5.50	5.49	5.51	5.46
	B [GPa]	85.54	86.91	85.14	82.23	84.03	87.01	82.71
	E_{coh} [eV]	-16.44	-16.34	-18.88	-16.88	-17.03	-13.94	-16.08
	E_{lat} [eV]	-26.90	-26.71	-28.42	-26.89	-26.99	-26.83	-27.46
SrF_2	a [Å]	5.85	5.81	5.67	5.84	5.83	5.87	5.80
	B [GPa]	63.09	68.08	88.72	61.91	61.39	65.91	69
	E_{coh} [eV]	-16.63	-16.51	-18.90	-17.01	-17.18	-14.30	-15.95
	E_{lat} [eV]	-25.33	-25.20	-26.81	-25.35	-25.44	-25.30	-26.03
BaF_2	a [Å]	6.26	6.22	6.06	6.24	6.23	6.31	6.20
	B [GPa]	61.25	64.94	73.34	62.36	63.49	53.87	57
	E_{coh} [eV]	-17.53	-17.38	-19.73	-17.90	-18.07	-15.10	-16.01
	E_{lat} [eV]	-23.79	-23.73	-25.31	-23.90	-24.00	-23.66	-24.58

oride crystals at finite conditions of temperature and pressure. Due to the absence of good catalytic properties for ZnF_2-based nanomaterials, I switched my investigations to other metal fluorides, namely CaF_2, SrF_2 and BaF_2, which are synthesized by our experimental partners in a sol-gel procedure [26, 27, 55]. These materials, of cubic fluorite structure, have revealed outstanding properties and are therefore mainly useful in optics, catalysis and dentistry [26, 27, 39, 57]. Starting with the bulk structure, I have recalled the ground state bulk properties of MF_2 (M = Ca, Sr and Ba) applying various DFT functionals. I calculated the lattice parameter, the bulk modulus, the cohesive energy and the lattice energy of the three systems. The results for the optimised bulk parameters obtained using Hartree-Fock and five different DFT functionals are shown in table 5.2. The Hartree-Fock method as well as all DFT functionals used were found to describe the bulk properties reasonably well. Best agreement with experiment was achieved at the PBE level which overestimates the lattice constant at most by 0.7% and underestimates the bulk modulus by 10% only (in the case of BaF_2, the bulk modulus is overestimated by 8%). The cohesive energy is slightly overestimated by at most 11% and the lattice energy is underestimated by 3%. Hence, I used the PBE functional in further calculations.

Surfaces in solids are usually created from the three-dimensionally bulk crystal by cutting along the Miller indices, and they are therefore described by these cutting planes. For the discussion of surface stabilities and the relative importance of different surfaces in a MF_2 crystal, we performed, in Paper P3, periodic slab calculations for three low-index surfaces: the (111) which is the natural cleavage plane of a fluorite structured crystal, the (110) and

the (100) surfaces. Using the slab model described in Chapter 3, the surface energy of the three mentioned surfaces was calculated with PBE for the materials under study. The (111) surface was found to be the most stable, followed by (110) and (100), in agreement with the experimental cleavage energies measured for the three considered materials [91, 201]. Due to the big energy difference between the (111) surface and the two other less stable surfaces, the latter did not appear in the Wulff construction of a MF_2 crystal; thus, only the (111) surface was exposed and the predicted shape of a MF_2 crystal in vacuum is an octahedron. This is only valid for a crystal in vacuum, where no temperature and gas pressure effects are included. However, MF_2 nanocrystals are synthesized under standard conditions of temperature and pressure, where they are in contact with a gaseous hydrogen fluoride phase. Hence, it is sensible to investigate the influence of temperature and HF pressure on the relative stability of low index MF_2 surfaces and consequently predict the most stable shapes of the nanocrystals at different synthetic conditions. To this end, we combined, in Paper P3, density functional theory and ab initio surface thermodynamics to analyze the stability of different surfaces and determine the presumable morphology of the crystals under various temperatures and HF concentrations. Surface energies were obtained as a function of the partial pressure of HF at four temperature conditions. For each material, the three low index planes (111), (110) and (100) were considered, each of them as a plain surface and covered with 100%, 50% and 25% HF. For the evaluation of surface energies of the HF covered terminations, we had to perform periodic DFT calculations for the adsorption of HF on the surfaces, at different coverages. We found that clean surfaces are most stable at very low HF pressure, while surfaces covered with HF are stabilized with increasing the pressure of HF. However, at high temperatures (T = 600K), even at a partial HF pressure as high as 1atm, still clean surfaces are dominant and a much higher pressure would be required to stabilize HF adsorption on the surfaces. Based on the surface energies of the different planes, Wulff plots of MF_2 crystals have been constructed for twelve sets of temperature and pressure conditions. These include temperatures of 150, 300, 450 and 600K and HF pressures of 10^{-10}, 10^{-5}, 1 and 10atm. Since at high temperatures clean surfaces are favored, as previously discussed, the shape of the crystals is very weakly affected by the variation of the HF pressure. This is not the case at low temperature, where adsorption structures are stabilized, resulting in different crystal shapes upon varying the pressure of the gas phase. The interpretations of the crystal shapes are discussed in detail for each metal fluoride in Paper P3. In general, all three materials were found to expose clean surfaces at high temperature and surfaces covered with HF at low temperature. In all cases, the (110) surface was not exposed, the (111) surface occured in eight facets resulting in an octaheral shape of the crystal whenever it is mainly exposed and the (100) surface, if mainly exposed, occured in six facets which correspond to a cubic shape. At room temperature and high excess of HF, CaF_2 nanocrystals were found to have a cubic shape, while octahedral nanocrystals were predicted for SrF_2 and BaF_2.

CaF_2 and SrF_2 nanocrystals have been synthesized at room temperature under large excess of HF and characterized with transmission electron microscopy (TEM), by our experimental collaborators. A distinct cubic shape was observed for CaF_2 nanocrystals, in agreement with

the theoretical prediction, whereas SrF_2 nanocrystals showed a more spherical shape, which can be idealized by the theoretical predicted octahedral shape. In general, the TEM images obtained experimentally support the theoretical findings.
Evaluating the reactivity of metal fluorides is crucial for the understanding of their application and use in surface science. Towards this direction, we aimed, in Paper P4, at thoroughly discussing the energetic and structural properties of HF adsorption, which was modeled at the PBE level and was used in the surface thermodynamics calculations of Paper P3. The use and comparison of different coverages were essential for examining the effect of the interactions among the adsorbed HF molecules on the adsorption structures and energies. In addition to the PBE calculated structures and energies, Hartree-Fock, PBE0, and dispersion corrected PBE calculations were performed in Paper P4, where the performance of the different methods was discussed. Adsorption structures were optimized at the Hartree-Fock, PBE and PBE0 levels, resulting in similar structures, while no struture optimization was performed at the DFT-D3 level. We found that the two DFT functionals used perform similarly for the adsorption of HF on the surfaces, with the PBE functional yielding slightly higher adsorption energies in most cases. Hartree-Fock was found to yield lower adsorption energies, and the highest energy values were calculated with dispersion correction to PBE. The PBE calculated adsorption energies were in the range of -0.4 to -1.7eV, implying a chemisorption of hydrogen fluoride on the surfaces in most cases. This is also confirmed by the optimized adsorption structures, in which the HF molecules were strongly bound to the surface, forming hydrogen bonds with the surface fluorines. Upon lowering coverage from full to half, the adsorption energies increase by up to 0.7eV. This increase is due to the minimization of the destabilizing interaction between the adsorbates.
After having completed this comprehensive study on metal fluoride surfaces, an insight was won in the aspects behind the catalytic activity of nanoscopic metal fluorides and the suitable experimental conditions responsible of obtaining a desired shape of the nanomaterial. For a more intuitive understanding of the lack in catalytic activity of ZnF_2, the next step would be the modeling of the defects in a ZnF_2 crystal, since the latter possesses a high density of them. A modeling within the periodic scheme is challenging, a cluster model would rather be more convenient. In the latter, the innermost part of the system, which is called cluster, contains the defect with a finite number of electrons and it is treated quantum mechanically. The outer part of the cluster is described by a periodic array of point charges.

Bibliography

[1] R. Feynamn, *J. Microelectromechanical Syst.* **1992**, *1*, 60–66.

[2] R. Birringer, H. Gleiter, H. P. Klein, P. Marquardt, *Phys. Lett. A* **1984**, *102*, 365–369.

[3] C. Murray, C. Kagan, M. Bawendi, *Ann. Rev. Mater. Sci.* **2000**, *30*, 545–610.

[4] A. Kosmala, R. Wright, Q. Zhang, P. Kirby, *Mater. Chem. Phys.* **2011**, *129*, 1075–1080.

[5] M. Holzinger, A. L. Goff, S. Cosnier, *Front. Chem. 2* **2014**, *63*, 1–10.

[6] B. L. Cushing, V. L. Kolesnichenko, C. J. O'Connor, *Chem. Rev.* **2004**, *104*, 3893–3946.

[7] J. E. Millstone, D. F. J. Kavulak, C. H. Woo, T. W. Holcombe, E. J. Westling, A. L. Briseno, M. F. Toney, J. M. J. Fréchet, *Langmuir* **2010**, *26*, 13056–13061.

[8] N. G. Khlebtsov, L. A. Dykman, *J. Quant. Spectrosc. Radiat. Transf.* **2010**, *111*, 1–35.

[9] S. Unser, I. Bruzas, J. He, L. Sagle, *Sensors* **2015**, *15*, 15684–15716.

[10] A. Loureiro, N. G. Azoia, A. C. Gomes, A. Cavaco-Paulo, *Curr. Pharm. Des.* **2016**, *22*, 1371–1390.

[11] E. Martis, R. Badve, M. Degwekar, *Chron. Young Sci.* **2012**, *3*, 68–73.

[12] A. P. Nikalje, *Med. Chem. 5* **2015**, *5*, 81–89.

[13] J. Yi, W. Robert, J. Molt, G. M. Blackburn, *Top. Curr. Chem. (Z)* **2017**, *375*, 1–31.

[14] Y. Lee, H. Sun, M. J. Young, S. M. George, *Chem. Mater.* **2016**, *28*, 2022–2032.

[15] F. Wang, S. W. Kim, D. H. Seo, K. Kang, L. Wang, D. Su, J. J. Vago, J. Wang, J. Graetz, *Nature Comm.* **2015**, *6*, 6668.

[16] M. V. Reddy, G. V. Subba Rao, B. V. R. Chowdari, *Chem. Rev.* **2013**, *113*, 5364–5457.

[17] X. Yu, T. J. Marks, A. Facchetti, *Nature Materials* **2016**, *15*, 383–396.

[18] R. J. Toh, Z. Sofer, M. Pumera, *ChemPhysChem* **2015**, *16*, 3527–3531.

[19] S. Rüdiger, E. Kemnitz, *Dalton Trans.* **2008**, 117–1127.

[20] E. Kemnitz, U. Groß, S. Rüdiger, S. C. Shakar, *Angew. Chem. Int. Ed.* **2003**, *42*, 4251–4254.

[21] S. Rüdiger, U. Groß, M. Feist, H. A. Prescott, S. C. Shakar, S. I. Troyanov, E. Kemnitz, *J. Mater. Chem.* **2005**, *15*, 588–597.

[22] S. Rüdiger, U. Groß, E. Kemnitz, *J. Fluorine Chem.* **2007**, *128*, 353–368.

[23] M. Nickkho-Amiry, G. Eltanany, S. Wuttke, S. Rüdiger, E. Kemnitz, J. M. Winfield, *J. Fluorine Chem.* **2008**, *129*, 366–375.

[24] E. Kemnitz, *Catal. Sci. Technol.* **2015**, *5*, 786–806.

[25] Y. Guo, S. Wuttke, A. Vimont, M. Daturi, J. C. Lavalley, K. Teinz, E. Kemnitz, *J. Mater. Chem.* **2012**, *22*, 14587.

[26] A. Rehmer, K. Scheurell, E. Kemnitz, *J. Mater. Chem. C* **2015**, *3*, 1716–1723.

[27] L. Schmidt, F. Emmerling, H. Kirmse, E. Kemnitz, *RSC Adv.* **2014**, *4*, 32–38.

[28] Private Communications, Kemnitz.

[29] N. Candu, S. Wuttke, E. Kemnitz, S. M. Coman, V. I. Parvulescu, *Appl. Catal. A* **2011**, *391*, 169–174.

[30] S. M. Coman, S. Wuttke, A. Vimont, M. Daturi, E. Kemnitz, *Adv. Synth. Catal.* **2008**, *350*, 2517–2524.

[31] S. M. Coman, V. I. Parvulescu, S. Wuttke, E. Kemnitz, *ChemCatChem* **2010**, *2*, 92–97.

[32] A. Negoi, S. Wuttke, E. Kemnitz, D. Macovei, V. I. Parvulescu, C. M. Teodorescu, S. M. Coman, *Angew. Chem. Int. Ed.* **2010**, *49*, 8134–8138.

[33] S. M. Coman, P. Patil, S. Wuttke, E. Kemnitz, *Chem. Commun.* **2009**, 460–462.

[34] S. B. Troncea, S. Wuttke, E. Kemnitz, S. M. Coman, V. I. Parvulescu, *Appl. Catal. B* **2011**, *107*, 260–267.

[35] E. Kemnitz, S. Wuttke, S. M. Coman, *Eur. J. Inorg. Chem* **2011**, 4773–4794.

[36] H. A. Prescott, Z.-J. Li, E. Kemnitz, J. Deutsch, H. Lieske, *J. Mater. Chem* **2005**, *15*, 4616–4628.

[37] S. Wuttke, S. M. Coman, J. Kröhnert, F. C. Jentoft, E. Kemnitz, *Catal. Today* **2010**, *152*, 2–10.

[38] A. Astruc, C. Cochon, S. Dessources, S. Celerier, S. Brunet, *Appl. Catal. A: General* **2013**, *453*, 20–27.

[39] H. Krüger, A. Hertwig, U. Beck, E. Kemnitz, *Thin Solid Films* **2010**, *518*, 6080–6086.

[40] J. Noack, L. Schmidt, H. G. Gläsel, M. Bauer, E. Kemnitz, *Nanoscale* **2011**, *3*, 4774–4779.

[41] D. R. Lide, *Handbook of Chemistry and Physics*, CRC Press, Boca Raton, **2003-2004**.

[42] S. Fujihara, Y. Kadota, T. Kimura, *J. Sol-gel Sci. Technol.* **2002**, *24*, 147–154.

[43] B. C. Hong, C. Kawano, *J. Alloys. Compd.* **2006**, *838*, 408–412.

[44] B. C. Hong, C. Kawano, *Opt. Mater.* **2008**, *30*, 952.

[45] P. T. Patil, A. Dimitrov, J. Radnikb, E. Kemnitz, *J. Mater. Chem.* **2008**, *18*, 1632.

[46] G. A. Kumar, C. W. Chen, J. Ballato, R. E. Riman, *Chem. Mater.* **2007**, *19*, 1523.

[47] X. Zhang, Z. Quan, J. Yang, P. Yang, H. Lian, J. Lin, *Nanotechnology* **2008**, *19*, 075603.

[48] A. Bensalah, M. Mortier, G. Patriarche, P. Gredin, D. Vivien, *J. Sol. State Chem.* **2006**, *179*, 2636–2644.

[49] X. Sun, Y. Li, *Chem. Commun.* **2003**, *14*, 1768–1769.

[50] F. Wang, X. Fan, D. Pi, M. Wang, *Sol. State Comm.* **2005**, *133*, 775–779.

[51] S. M. Chauhan, B. S. Chakrabarti, *Int. J. Eng. Res. & Technol.* **2014**, *3*, 129–131.

[52] L. Wang, B. Wang, X. Wang, W. Lu, *Opt. Mater.* **2007**, *29*, 1179–1185.

[53] K. Tahvildari, M. E. Pour, S. Ghammamy, H. Nabipour, *Int. J. Nano Dim.* **2012**, *2*, 269–273.

[54] G. S. M. Dreger, E. Kemnitz, *Sol. State Sci.* **2011**, *14*, 528–534.

[55] U. Groß, S. Rüdiger, E. Kemnitz, *Sol. State Sci.* **2007**, *9*, 838–842.

[56] Z. Kaawar, S. Mahn, E. Kemnitz, B. Paulus, *Molecules* **2017**, *22*.

[57] K. Teinz, S. Wuttke, F. Börno, J. Eicher, E. Kemnitz, *Journal of Catalysis* **2011**, *282*, 175–182.

[58] S. Kobayashi, T. Hamada, K. Manabe, *J. Am. Chem. Soc.* **2002**, *124*, 5640–5641.

[59] T. Roth, *J. Appl. Phys.* **1973**, *44*, 1056.

[60] A. G. Banshchikov, N. F. Kartenko, A. K. Kaveev, M. M. Moisseeva, N. S. Sokolov, *Proc. SPIE 5023* **2002**, *19*.

[61] M. Noboru, S. Takashi, M. Hironaga, N. Ryotaro, *Japanese Journal of Applied Physics* **1992**, *31*, 51.

[62] W. Pong, S. K. Okada, *Phys. Rev. B* **1979**, *19*, 5307–5309.

[63] K. Kawano, T. Ohya, T. Tsurumi, K. Katoh, R. Nakata, *Phys. Rev. B* **1999**, *60*, 11984.

[64] A. P. Ayala, *J. Phys.: Condens. Matter* **2001**, *13*, 11741.

[65] N. Sata, K. Eberman, K. Eberl, J. Maier, *Nature* **2000**, *408*, 946.

[66] I. H. Malitson, *Appl. Opt.* **1963**, *2*, 1103–1107.

[67] A. Ikesue, Y. L. Aung, *Nat. Photonics* **2008**, *2*, 721–727.

[68] L. Ling, X. Xu, G. Y. Choi, D. Billodeaux, G. Guo, R. M. Diwan, *J. Dent. Res.* **2009**, *88(1)*, 83–88.

[69] H. H. K. Xu, J. L. Moreau, L. Sun, L. C. Chow, *J. Dent. Res.* **2010**, *89(7)*, 739–745.

[70] N. J. O'Toole, V. A. Streltsov, *Acta Crystallogr. Sect. B* **2001**, *57*, 128.

[71] A. Perakis, D. Lampakis, Y. Boulmetis, C. Raptis, *Phys. Rev. B* **2002**, *72*, 144108.

[72] S. Torabi, L. Hammerschmidt, E. N. Voloshina, B. Paulus, *Int. J. Quantum Chem.* **2014**, *114*, 943–951.

[73] J. Barth, R. L. Johnson, M. Cardona, D. Fuchs, A. M. Bradshaw, *Phys. Rev. B* **1990**, *41*, 3291.

[74] P. Camy, J. L. Doualan, S. Renard, A. Braud, V. Menard, R. Moncorge, *Opt. Commun* **2004**, *236*, 395.

[75] G. A. Kumar, R. Riman, S. C. Chae, Y. N. Yang, I. K. Bae, H. S. Moon, *J. Appl. Phys.* **2004**, *95*, 3243.

[76] T. Tsujibayashi, K. Toyoda, S. Sakuragi, M. Kamada, M. Itoh, *Appl. Phys. Lett.* **2002**, *80*, 2883.

[77] F. Giessibl, M. Reichling, *Nanotechnology* **2005**, *16*, S118–S124.

[78] E. Morris, T. Groy, K. Leinenweber, *J. Phys. Chem. Solids* **2001**, *62*, 1117.

[79] R. C. Weast, *CRC Handbook of Chemistry and Physics*, CRC Press, Boca Raton, **1976**.

[80] M. Nicolav, *J. Cryst. Growth* **2000**, *218*, 62.

[81] G. A. Samara, *Phys. Rev. B* **1976**, *13*, 4529.

[82] R. W. G. Wyckoff, *Crystal Structures, 2nd Edition, Vol. 1*, Interscience Publishers, New York, **1982**.

[83] J. M. Leger, J. Haines, A. Atouf, O. Schuete, S. Hull, *Phys. Rev. B* **1995**, *52*, 13247.

[84] L. Gerward, J. S. Olsen, S. Steenstrup, M. Malinowski, S. Asbrink, A. Waskowska, *J. Appl. Cryst.* **1992**, *25*, 578.

[85] V. Kanchana, G. Vaitheeswaran, M. Rajagopalan, *Physica B* **2003**, *328*, 283.

[86] V. Kanchana, G. Vaitheeswaran, M. Rajagopalan, *J. Alloys and Comp.* **2003**, *359*, 66.

[87] G. W. Rubloff, *Phys. Rev. B* **1972**, *5*, 662.

[88] H. Shi, R. I. Eglitis, G. Borstel, *Phys. Stat. Sol. (b)* **2005**, *242*, 2041.

[89] H. Shi, R. I. Eglitis, G. Borstel, *J. Phys. Condens. Matter* **2006**, *18*, 8367.

[90] R. Bennewitz, M. Reichling, E. Matthias, *Surf. Sci.* **1997**, *387*, 69.

[91] J. J. Gilman, *J. Appl. Phys.* **1960**, *31*, 2208.

[92] P. B. Barraclough, P. G. Hall, *J. Chem. Soc. Faraday Trans. 1* **1975**, *71*, 2266–2276.

[93] N. H. de Leeuw, T. G. Cooper, *J. Mater. Chem.* **2003**, *13*, 93.

[94] H. Lüth, *Surfaces and Interfaces of Solid Materials*, Springer, **1995**.

[95] R. Valero, J. R. B. Gomes, D. G. Truhlar, F. Illas, *J. Chem. Phys.* **2010**, *132*, 104701.

[96] I. Z. Koleva, H. A. Aleksandrov, G. N. Vayssilov, R. Duarteb, J. A. van Bokhoven, *Phys. Chem. Chem. Phys.* **2015**, *17*, 22389.

[97] S. Kristyán, P. Pulay, *Chem. Phys. Lett.* **1994**, *229*, 175.

[98] P. Hobza, J. Sponer, T. Reschel, *J. Comput. Chem.* **1995**, *16*, 1315.

[99] J. M. Pérez-Jordá, A. D. Becke, *Chem. Phys. Lett.* **1995**, *233*, 134.

[100] J. M. Pérez-Jordá, E. San-Fabián, A. J. Pérez-Jiménez, *J. Chem. Phys.* **1999**, *110*, 1916.

[101] W. Chen, C. Tegenkamp, H. Pfnur, T. Bredow, *Phys. Chem. Chem. Phys.* **2009**, *11*, 9337.

[102] Y. Anderson, D. C. Langreth, B. I. Lundqvist, *Phys. Rev. Lett.* **1996**, *76*, 102–105.

[103] D. C. Langreth, M. Dion, H. Rydberg, E. Schröder, P. Hyldgaard, B. I. Lundqvist, *Int. J. Quantum Chem.* **2005**, *101*, 599–610.

[104] T. Sato, T. Tsuneda, K. Hirao, *Mol. Phys.* **2005**, *103*, 1151–1164.

[105] O. A. von Lilienfeld, I. Tavernelli, U. Rothlisberger, D. Sebastiani, *Phys. Rev. Lett.* **2004**, *93*, 153004.

[106] Y. Y. Sun, Y. H. Kim, K. Lee, S. B. Zhang, *J. Chem. Phys.* **2008**, *129*, 154102.

[107] Y. Zhao, D. G. Truhlar, *Acc. Chem. Res.* **2008**, *41*, 157–167.

[108] S. Grimme, *J. Comput. Chem.* **2006**, *27*, 1787–1799.

[109] S. Grimme, J. Antony, S. Ehrlich, H. Krieg, *J. Chem. Phys.* **2010**, *132*, 154104.

[110] B. Civalleri, L. Maschio, P. Ugliengo, C. Zicovich-Wilson, *Phys. Chem. Chem. Phys.* **2010**, *12*, 6382.

[111] A. Boese, J. Sauer, *Phys. Chem. Chem. Phys.* **2013**, *15*, 16481.

[112] J. P. Ramalho, J. Gomes, F. Illas, *RSC Adv.* **2013**, *3*, 13085.

[113] A. Rimola, D. Costa, M. Sodupe, J.-F. Lambert, P. Ugliengo, *Chem. Rev.* **2013**, *113*, 4216.

[114] A. Szabo, N. S. Ostlund, *Modern Quantum Chemistry*, 1st ed., Dover Publication, Inc, Mineola, NewYork, **1996**.

[115] J. Cizek, *Adv. Chem. Phys.* **1969**, *14*, 35.

[116] C. Møller, M. S. Plesset, *Phys. Rev.* **1934**, *46*, 618–622.

[117] C. Müller, B. Paulus, *Phys. Chem. Chem. Phys.* **2012**, *14*, 7605–7614.

[118] G. Stollhoff, P. Fulde, *Z. Phys. B* **1977**, *26*, 257–262.

[119] G. Stollhoff, P. Fulde, *J. Chem. Phys.* **1980**, *73*, 4548–4561.

[120] G. Stollhoff, *J. Chem. Phys.* **1996**, *105*, 227–234.

[121] P. Pulay, *Chem. Phys. Lett.* **1983**, *100*, 151–154.

[122] P. Pulay, S. Saebø, *Theoretica Chimica Acta* **1986**, *69*, 357–368.

[123] S. Saebø, P. Pulay, *J. Chem. Phys.* **1987**, *86*, 914–921.

[124] H.-J. Werner, P. J. Knowles, G. Knizia, F. R. Manby, M. Schütz, P. Celani, W. Györffy, D. Kats, T. Korona, R. Lindh, A. Mitrushenkov, G. Rauhut, K. R. Shamasundar, T. B. Adler, R. D. Amos, A. Bernhardsson, A. Berning, D. L. Cooper, M. J. O. Deegan, A. J. Dobbyn, F. Eckert, E. Goll, C. Hampel, A. Hesselmann, G. Hetzer, T. Hrenar, G. Jansen, C. Köppl, Y. Liu, A. W. Lloyd, R. A. Mata, A. J. May, S. J. McNicholas, W. Meyer, M. E. Mura, A. Nicklass, D. P. O'Neill, P. Palmieri, D. Peng, K. Pflüger, R. Pitzer, M. Reiher, T. Shiozaki, H. Stoll, A. J. Stone, R. Tarroni, T. Thorsteinsson, M. Wang, MOLPRO, version 2015.1, a package of ab initio programs.

[125] H. J. Werner, P. J. Knowles, G. Knizia, F. R. Manby, M. Schütz, *WIREs Comput. Mol. Sci.* **2012**, *2*, 242–253.

[126] C. Pisani, L. Maschio, S. Casassa, M. Halo, M. Schütz, D. Usvyat, *J. Comput. Chem.* **2008**, *29*, 2113.

[127] C. Pisani, M. Busso, G. Capecchi, S. Casassa, R. Dovesi, L. Maschio, C. Zicovich-Wilson, M. Schütz, *J. Chem. Phys.* **2005**, *122*, 094113.

[128] C. Pisani, M. Schütz, S. Casassa, D. Usvyat, L. Maschio, M. Lorenz, A. Erba, *Phys. Chem. Chem. Phys.* **2012**, *14*, 7615–7628.

[129] H. Stoll, *Chem. Phys. Lett.* **1992**, *191*, 548.

[130] H. Stoll, *J. Chem. Phys.* **1992**, *97*, 8449.

[131] H. Stoll, *Phys. Rev. B* **1992**, *46*, 6700.

[132] B. Paulus, *Phys. Rep.* **2006**, *428*, 1.

[133] L. Hammerschmidt, C. Müller, B. Paulus, *J. Chem. Phys.* **2012**, *136*, 124117.

[134] K. Reuter, M. Scheffler, *Phys. Rev. B* **2001**, *65*, 035406.

[135] P. Geysermans, F. Finocchi, J. Goniakowski, R. Hacquart, J. Jupille, *Phys. Chem. Chem. Phys.* **2008**, *11*, 2228–2233.

[136] C. Stampfl, H. J. Kreuzer, S. H. Payne, H. Pfnür, M. Scheffler, *Phys. Rev. Lett.* **1999**, *83*, 2993–2996.

[137] J. Rogal, K. Reuter, M. Scheffler, *Phys. Rev. B* **2004**, *69*, 075421.

[138] C. Bailey, S. Mukhopadhyay, A. Wander, B. Searle, N. Harrison, *J. Phys. Chem. C* **2009**, *113*, 4976.

[139] E. Kanaki, S. Gohr, C. Müller, B. Paulus, *Surf. Sci.* **2015**, *632*, 158–163.

[140] M. Planck, *Annalen der Physik* **1901**, *309*, 553–563.

[141] M. Born, W. Heisenberg, P. Jordan, *Zeitschrift für Physik* **1926**, *35*, 557–615.

[142] E. Schrödinger, *Annalen der Physik* **1926**, *384*, 361–376.

[143] M. Born, R. Oppenheimer, *Annalen der Physik* **1927**, *389*, 457–484.

[144] D. R. Hartree, *Math. Proc. Camb. Phil. Soc.* **1928**, *24*, 89–110.

[145] J. C. Slater, *Phys. Rev.* **1929**, *34*, 1293–1322.

[146] V. Fock, *Z. Phys.* **1930**, *61*, 126–148.

[147] D. R. Hartree, V. Hartree, *P. Roy. Soc. Lond. Ser.-A* **1935**, *150*, 9–33.

[148] I. N. Levine, *Quant. Chem.* **2000**.

[149] C. C. J. Roothaan, *Rev. Mod. Phys.* **1951**, *23*, 69–89.

[150] G. G. Hall, *Proc. R. Soc. Lond. A* **1951**, *205*, 541–552.

[151] E. Schrödinger, *Annalen der Physik* **1926**, *385*, 437–490.

[152] L. H. Thomas, *Math. Proc. Camb. Phil. Soc.* **1927**, *23*, 542–548.

[153] E. Fermi, *Z. Phys.* **1928**, *48*, 73–79.

[154] P. Hohenberg, W. Kohn, *Phys. Rev.* **1964**, *136*, B864–B871.

[155] V. Kohn, L. J. Sham, *Phys. Rev.* **1965**, *140*, A1133–A1138.

[156] P. A. M. Dirac, *Math. Proc. Camb. Phil. Soc.* **1930**, *26*, 376–385.

[157] J. C. Slater, *Phys. Rev.* **1951**, *81*, 385–390.

[158] S. H. Vosko, L. Wilk, M. Nusair, *Can. J. Phys.* **1980**, *58*, 1200–1211.

[159] D. M. Ceperley, B. J. Alder, *Phys. Rev. Lett.* **1980**, *45*, 566–569.

[160] R. G. Parr, W. Yang, *Density functional theory of atoms and molecules* **1989**.

[161] J. P. Perdew, K. Burke, M. Ernzerhof, *Phys. Rev. Lett.* **1996**, *77*, 3865–3868.

[162] A. D. Becke, *Phys. Rev. A* **1988**, *38*, 3098–3100.

[163] C. Lee, W. Yang, R. G. Parr, *Phys. Rev. B: Condens. Matter* **1988**, *37*, 785–789.

[164] J. P. Perdew, Y. Wang, *Phys. Rev. B* **1992**, *45*, 13244–13249.

[165] Q. Wu, W. Yang, *J. Chem. Phys.* **2002**, *116*, 515.

[166] N. W. Ashcroft, D. N. Mermin, *Sol. State Phys.* CBS Publishing ASIA LTD, Philadelphia, **1976**.

[167] R. Dovesi, B. Civalleri, C. Roetti, V. R. Saunders, R. Orlando, *Ab Initio Quantum Simulation in Solid State Chemistry*, (Eds.: L. R. ed. L. K. B., C. T. R.), vol. 21, ch.1, pp. 1-125, John Wiley & Sons, Inc., **2005**.

[168] F. Bloch, *Z. Phys.* **1929**, *52*, 555–600.

[169] C. Pisani, *Quantum-Mechanical Ab-initio calculations of the Properties of Crystalline Materials*, Springer Verlag: Heidelberg, **1996**.

[170] J. M. André, L. Gouverneur, G. Leroy, *Int. J. Quantum Chem.* **1967**, *1*, 427.

[171] J. M. André, L. Gouverneur, G. Leroy, *Int. J. Quantum Chem.* **1967**, *1*, 451.

[172] J. M. André, *J. Chem. Phys.* **1969**, *50*, 1536.

[173] J. Hafner, *J. Comput. Chem.* **2008**, *29*, 2044–2078.

[174] V. R. Saunders, C. F. Feva, R. Dovesi, L. Salasco, C. Roetti, *Mol. Phys.* **1992**, *77*, 629–665.

[175] R. Dovesi, R. Orlando, B. Civalleri, C. Roetti, V. R. Saunders, C. M. Zicovich-Wilson, *Z. Kristallogr.* **2005**, *220*, 571–573.

[176] R. Dovesi, V. Saunders, C. Roetti, R. Orlando, C. M. Zicovich-Wilson, F. Pascale, B. Civalleri, K. Doll, N. Harrison, I. Bush, P. D'Arco, M. Llunell, CRYSTAL09 User's Manual, University of Torino, Torino, **2010**.

[177] S. Saebø, P. Pulay, *Annu. Rev. Phys. Chem.* **1993**, *44*, 213–236.

[178] M. Schütz, G. Hetzer, H. J. Werner, *J. Chem. Phys.* **1999**, *111*, 5691–5705.

[179] C. M. Zicovich-Wilson, R. Dovesi, V. R. Saunders, *J. Chem. Phys.* **2001**, *115*, 9708–9719.

[180] S. Casassa, C. M. Zicovich-Wilson, C. Pisani, *Theor. Chem. Acc.* **2006**, *116*, 726–733.

[181] C. M. Zicovich-Wilson, A. Bert, C. Roetti, R. Dovesi, V. R. Saunders, *J. Chem. Phys.* **2002**, *116*, 1121.

[182] G. H. Wannier, *Phys. Rev.* **1937**, *52*, 191–197.

[183] L. Maschio, D. Usvyat, *Phys. Rev. B* **2008**, *78*, 73102.

[184] C. Pisani, G. Capecchi, S. Casassa, L. Maschio, *Mol. Phys.* **2005**, *103*, 2527–2536.

[185] D. A. McQuarrie, J. D. Simon, *Physical Chemistry a molecular approach* **1997**.

[186] J. W. Gibbs, *Collected Works* **1928**.

[187] E. A. Guggenheim, *Trans. Faraday Soc.* **1940**, *35*, 397–412.

[188] J. W. Gibbs, *Transactions of the Connecticut Academy of Arts and Sciences* **1876**, *3*, 108–248.

[189] G. Wulff, *Zeitschrift für Kristallographie und Mineralogie* **1901**, *34*, 449–530.

[190] A Wulff plot, `https://upload.wikimedia.org/wikipedia/commons/thumb/c/ce/Wulff_construction.svg/256px-Wulff_construction.svg.png`.

[191] H. B. Jansen, P. Ros, *Chem. Phys. Lett.* **1969**, *3*, 140.

[192] B. Liu, A. D. McLean, *J. Chem. Phys.* **1973**, *59*, 4557.

[193] S. F. Boys, F. Bernardi, *Mol. Phys.* **1970**, *19*, 553.

[194] M. Kaupp, P v R. Schleyer, H Stoll, H Preuss, *J. Chem. Phys.* **1991**, *94*, 1360.

[195] D. Belger, Z. Huesges, E. Voloshina, B. Paulus, *J. Phys.: Condens. Matter* **2010**, *22*, 275504.

[196] D. Figgen, G. Rauhut, M. Dolg, H. Stoll, *Chem. Phys.* **2005**, *311*, 227–244.

[197] A. Erba, M. Halo, *Beyond Standard Quantum Chemsitry: from Molecules to Extended Systems*, (Transworld Research Network), **2007**.

[198] http://webbook.nist.gov/chemistry.

[199] J. D. Cox, D. D. Wagman, V. A. Medvedev, CODATA Key Values For Thermodynamics, Hemisphere Publ, **1989**.

[200] Z. Huesges, C. Müller, B. Paulus, L. Maschio, *Surf. Sci.* **2014**, *627*, 11–15.

[201] P. Kraatz, T. Zoltai, *J. Appl. Phys.* **1974**, *45*, 4741.